The falling sphere problem and capturing enhanced drag with Boger fluids

I.E. Garduño , H.R. Tamaddon-Jahromi , M.F. Webster

PII: S0377-0257(16)00053-7
DOI: 10.1016/j.jnnfm.2016.02.009
Reference: JNNFM 3759

To appear in: *Journal of Non-Newtonian Fluid Mechanics*

Received date: 19 October 2015
Revised date: 21 February 2016
Accepted date: 23 February 2016

Please cite this article as: I.E. Garduño , H.R. Tamaddon-Jahromi , M.F. Webster , The falling sphere problem and capturing enhanced drag with Boger fluids, *Journal of Non-Newtonian Fluid Mechanics* (2016), doi: 10.1016/j.jnnfm.2016.02.009

Highlights

- Enhanced drag resolved for different geometry aspect ratios with a swanINNFM model
- Experimental drag measurements have been quantitatively captured
- At fixed elasticity, there is increase in drag with rise in solvent fraction
- Transition phases are detected between steady, oscillatory, and unstable solutions
- Flow-rate increase exhibits larger *drag* compared to fluid-relaxation time increase

The falling sphere problem and capturing enhanced drag with Boger fluids

I.E. Garduño, H.R. Tamaddon-Jahromi, M.F. Webster*

Institute of Non-Newtonian Fluid Mechanics Swansea University Bay Campus, College of Engineering, Fabian Way Swansea, SA1 8EN, UK

Abstract

In this computational study, the ability of an extensional White–Metzner construction with the FENE-CR model is considered to reflect experimental enhanced drag data of Jones *et al.* [1]. The numerical drag predictions for three different aspect ratios of sphere:tube radii {0.5, 0.4, 0.2} are obtained with a hybrid finite element/volume (*fe/fv*) algorithm. Excellent agreement is extracted for all three aspect ratios against the experimental measurements, and at any specified rate, the tighter-fitting the aspect ratio the lower the resulting drag. Moreover, as the Weissenberg number is increased, the transition between steady-state and oscillatory flow is recognised from the instantaneous pressure data, prior to numerical divergence. A main realisation in this study is that it is *important to select the same procedure* of *Wi*-continuation across experimental and computational protocols, to extract comparable levels of drag. Clearly the λ_1*-increase* mode (common computational form), is more involved than the *Q*-increase mode (usual experimental form), and as such, less robust as a reliable method for accurate drag prediction and enhanced drag capture. In general, flow-rate increase (*Q-increase*) conditions generate larger drag enhancement, when compared to fluid-relaxation time increase (λ_1*-increase*), at comparable levels of dissipative-factor (λ_D). The investigation also follows parametric variation in solvent fraction (β_{solvent}) in one particular geometric aspect-ratio instance. This reveals that at any specific fixed elasticity level, there is an increase in drag observed with rise in β_{solvent}. In addition, high solute/low-solvent fractions at low dissipative-factor, were only found to generate drag reduction, consistent with the literature. New and key facets to this *fe/fv* implementation are summarised, in appealing to: an improved velocity gradient boundary conditions imposed at the centreline (*VGR-correction*); continuity correction; absolute value of the stress-trace function (*ABS-f*-correction); increasing flow-rate solution continuation; alongside advanced techniques in *fv*-time discretisation, discrete treatment of pressure terms, and compatible stress/velocity-gradient representation.

Keywords: Viscoelastic fluid; FENE-CR; Extensional White-Metzner model (swanINNFM); Flow past a sphere; Drag coefficient

* Corresponding Author. *E-mail address:* m.f.webster@swansea.ac.uk

1. Introduction

This article tackles one of the fundamental grand-challenge problems in computational rheology that of predictive capture of enhanced drag observed for Boger fluids in the falling sphere experiment. State-of-the-art reviews well cover the topic in Walters and Tanner [2], Brown *et al*. [3], McKinley [4], Caswell *et al*. [5], and Chhabra [6]). Such an experiment (see Jones *et al*. [1]), may be conducted with varying diameter (2*R*) tubes and spheres (2*a*), to achieve increased terminal velocities at a fixed geometric aspect-ratio ($\beta_{\text{sphere}} = a / R$). Once the sphere achieves its terminal velocity, travelling along the centreline of the tube, the flow is then considered as *steady*. The relevant bounding fluid properties therefore reflect constant shear viscosity, extensional hardening yet finite extensibility, and a quadratic to less-than-quadratic first-normal stress-difference at larger shear rates. Notably, the extensional and normal-stress properties of the fluid are of crucial importance in detecting the all-important rheological influence upon the enhanced drag exerted on a sphere falling through a constant viscosity viscoelastic fluid of Boger-type, displaying strain-hardening properties.

On the experimental side, Jones *et al*. [1] studied two Boger fluids, termed Type-I and Type-II, with findings that have been used extensively for comparison throughout this investigation. For PIB/PB-based Boger fluid (Type-II), these authors have shown modest increase in drag coefficient to 1.3 with ($\beta_{\text{sphere}} = 0.5$) at Weissenberg number (*Wi*=1.35), noting intersection with the Newtonian reference line at *Wi*~0.625. As aspect ratio (β_{sphere}) declines (through values of 0.4 and 0.2) and at any fixed *Wi* up to ~1.30, such drag values are observed to elevate quite considerably. For example at *Wi*=1.30, a drag coefficient of 1.7 is achieved with β_{sphere} =0.4, and of 2.0 with β_{sphere} =0.2. For aspect ratio $\beta_{\text{sphere}} \leq 0.15$, the drag becomes independent of further aspect ratio adjustment (see below for more details). In addition, Becker *et al*. [7] examined the problem experimentally using a digital imaging system for an aspect ratio of (β_{sphere} =0.243) and a polyisobutylene (PIB) Boger fluid. The motion of the sphere was taken as accelerating from rest, falling down the centreline of a cylindrical tube. Transient numerical solutions (velocity profiles) were supplied through a Lagrangian finite element method whilst including inertia, using both single and multi-mode Oldroyd models. Experimentally, these authors observed large transient velocity overshoots of O(50%), prior to achieving terminal settling velocities. Becker *et al*. with single-mode representation, could not re-capture the large increases in steady-state drag-coefficient of Jones *et al*., noted for both Type-I and Type-II fluids (maximum drag-value, *K*=3.7), at comparable aspect-ratio of (β_{sphere} =0.25). Similarly, Becker *et al.* detected a maximum drag-value of *K*=2.4 by experiment, and *K*=2.2 by single-mode Oldroyd prediction at limiting *De*~3.4. One notes here that Jones *et al*., only detected O(30%) transient velocity overshoots, shown for Type-I fluids. Such differences in observational findings may be due to several factors, not least being – use of different fluids with varying properties and composition (networked structures, aging, densities of these fluids, zero shear-rate viscosities and relaxation times), and precise determination of terminal velocities. The authors acknowledge that the experimental measurements themselves are prone to error bars, and relatively small differences in raw drag enhancement can be distorted under relative drag-coefficient

reporting, due to adjustment in base K_N-values (Newtonian-drag) as aspect-ratio is altered. Furthermore, the multi-mode transient predictions of Becker *et al.*, with a four-mode Oldroyd model, under-predicted the evolution of the sphere-velocity, yet provided improved overall quantitative agreement with the experimental data over single-mode predictions, reducing the magnitude of discrepancy to the overshoot achieved. Nevertheless, similar levels of terminal velocity were approached at *steady-state* for single- and multi-mode solutions, comparable to the experimental data. Hence, the expectation is of similar levels of steady-state drag. Still, Becker *et al.* cite (Bird et al. 1987 [8]), in reference to transient representation, quoting that "*Although the Oldroyd-B model provides a reasonable description of the material functions for a Boger fluid in steady shearing flows, it is widely appreciated that the presence of a single relaxation time λ_1 renders the model incapable of quantitatively describing transient phenomena of real polymeric fluids, even in the linear viscoelastic limit*".

In a study performed over the polymer properties (solvent quality and polymer molecular weight), Solomon and Muller [9] concluded that the final drag on a sphere is determined by the interplay between the quality of the solvent, and the shear and extensional rheology of the solutions involved. Further discussion on this particular aspect can be found in Walters and Tanner [2] and McKinley [4].

This falling sphere problem has proven both classical and popular. Yet, despite the simplicity of the flow and the absence of geometric singularities, numerical simulations have proven conspicuously incapable of capturing the *enhanced drags* observed experimentally for these strain-hardening fluids, as described above. Many computational predictions report *only drag reduction*, and often prove limited in *steady-solution* acquisition to a critical elasticity level, governed by (Wi_{crit}), beyond which upturn in drag has remained an open question. This barrier to the lack of numerical convergence has been attributed in part to a number of issues - the complex mixture of shear and extensional flow regimes encountered (hence to the mathematical properties of the problem itself); problem discretisation and constitutive representation; and to the method of solution employed. Neither does shifting to a multi-mode representation, change this overall position. Hence, the discrepancy between the significant enhanced drag observed *experimentally*, and the under-prediction provided by *simulation* at high *Wi*-levels, has emerged as an outstanding computational issue to resolve (see the literature - Tiefenbruck and Leal [10], Gervang *et al*. [11], Mena *et al*. [12], Owens and Phillips [13], Chhabra [6]).

Caswell *et al.* [5] pointed out that this discrepancy, between experimental measurements and computed solutions, may be somewhat due to the inadequacy of the *constitutive models* used. As a consequence, various numerical schemes have been benchmarked on the standardised specification of the flow problem – that of the creeping motion of a sphere in a constant shear-viscosity viscoelastic fluid (generally, Oldroyd-B, single-mode), contained within a cylindrical tube with an aspect ratio of $\beta_{\text{sphere}} = 0.5$, (see for example, Brown *et al.* [3]; Tanner [14]; Owens and Phillips [15]). Moreover, Satrape *et al.* [16] performed a numerical study for this benchmark problem using a FENE-CR model. These authors concluded that the finitely-extensible dumbbell construction gave access to a somewhat larger range of *Wi*-values (as taken up in the present study).

Moreover, the magnitude of the solvent fraction (β_{solvent}, see definition below) was also found to regulate the faster or slower decrease of the drag as a function of *Wi*. In this regard, with $\beta_{\text{sphere}} = 0.5$ and for the Oldroyd-B model, Tamaddon-Jahromi *et al.* [17] presented a comparison of the drag versus elasticity increase (reported in Deborah number, *De*, here equivalent to *Wi*) for three alternative levels of solvent fraction (β_{solvent} =1/9, 0.5, 0.9) up to *Wi*=1.2. The results reflected a decreasing trend in drag across all three solvent fractions, with no sign of predicted enhancement. The authors concluded that at any specific fixed elasticity level, there is an increase in drag observed with rise in β_{solvent} ($\beta_{\text{solvent}} \to 1$). For cross-comparison purposes with the literature, the same authors also included the results of Bodart and Crochet [18], and Lunsmann *et al.* [19], where there is general consensus observed in drag results across methods and solvent fractions.

Further analysis for values of β_{solvent} =0.25 has revealed high stress levels, within the region between the sphere and the tube wall, larger in comparison to those in the wake region (Fan *et al.* [20]). Hence, it is widely acknowledged that $\beta_{\text{solvent}} = 0.5$ may not have been the optimal choice for the benchmark. This has lead to alternative β_{solvent}-ratios being proposed ($\beta_{\text{solvent}} = 0.125$ and 0.25, see Brown & McKinley [3]), even though for these ratios there is sparsity of experimental data to hand.

Lunsmann *et al*. [19] investigated the case $\beta_{\text{solvent}} = 0.125$ for a variety of constitutive equations obtaining good agreement between their corresponding numerical solutions for $Wi < 1.6$. In addition, Zheng *et al*. [21] used a similarity solution, in the neighbourhood of the tube-centreline through the wake region, and probed the existence of a limiting *Wi*-value (approximately 0.6, for an Oldroyd-B model). Nevertheless, none of these numerical solutions have captured drag enhancement, as in experimental findings for different instances of β_{solvent}. In addition, one of the major challenges offered by this particular problem has been to resolve steady-state solutions in such complex flow scenarios at relatively high levels of *Wi*. The lack of success in reaching high *Wi* has often been attributed to the sharp gradients in the polymeric stresses generated (progressive stimulation of ever-thinner stress boundary layers), that heighten with *Wi*-rise (Happel and Brenner [21]; Bodart and Crochet [18]; Zheng *et al.* [22], Owens and Phillips [13]). However, Petera [23] later found that stable steady-state numerical solutions could be reached up to *Wi*=6.6 with the UCM model, by using a Lagrangian particle-line scheme. This author observed that the drag factor (*K*) fell from the Newtonian reference value of 6.0 to a minimum of ~4.0, before levelling out and then showing a modest rise. This result gives some hope that numerical convergence issues may be overcome, and that some upturn in drag may be realised; nevertheless, this is still far from the desired enhanced drag position sought through prediction.

Our earlier work on the viscoelastic falling-sphere problem [17, 24] has considered various forms of constitutive representation for Boger fluids, such as constant viscosity Oldroyd-B, FENE-CR [25] and White-Metzner [26] models. In the present study, proceeding from the above background and to reflect enhanced drag for different problem aspect-ratios, the various properties are explored of the conformation of two constant shear-viscosity models - the White-Metzner

construction and the FENE-CR model. Hence, and primarily for a single geometric aspect-ratio ($\beta_{\text{solvent}} = 0.5$), solution parametric windows have been investigated to predict and encapsulate the available experimental data. This demonstrates the limitations of steady solution extraction, prior to an oscillatory solution phase and eventual solution instability. Subsequently, this position is then extended to alternative, more loosely-fitting aspect-ratios of $\beta_{\text{solvent}} = 0.25$ and 0.2, where a similar realisation is gathered. Finally, numerical solutions with adjustment in fluid solvent-fraction (β_{solvent}) are also considered, in one particular aspect-ratio instance ($\beta_{\text{solvent}} = 0.5$). This provides some insight and comparison upon the standard computational-benchmark drag-results provided for the problem-setting of $\beta_{\text{solvent}} = 1/9$ (low-solvent/high-solute).

Vital to the current algorithmic formulation and solution procedure are several new aspects. This includes: improved discrete velocity gradient treatment on the flow-centreline (VGR-correction); imposition of a correction for continuity; adopting the absolute form of the stress-structure function (*f*-ABS representation, [27]); increasing flow-rate through solution continuation; alongside advanced techniques in *fv* time-discretisation, discrete treatment of pressure terms, and compatible stress/velocity-gradient representation [28, 29].

2. Governing equations and flow problem

The flow problem is specified through the relevant equation system, given in non-dimensional terms, for isothermal, viscous, incompressible flow and represented via equations for conservation of mass and momentum transport, viz.

$$\nabla \cdot \mathbf{u} = 0, \tag{1}$$

$$Re\frac{\partial \mathbf{u}}{\partial t} = -Re\mathbf{u}\cdot\nabla\mathbf{u} + \nabla\cdot\boldsymbol{T} - \nabla p. \tag{2}$$

In the above, $\boldsymbol{T}$ is the stress, defined as $\boldsymbol{T} = \tau + 2\beta_{\text{solvent}}\mathbf{d}$. Field variables *u*, **d**, and *p* represent fluid velocity, the rate-of-deformation is $(\nabla\mathbf{u} + \nabla\mathbf{u}\dagger)/2$, and the hydrodynamic pressure, respectively. In addition, the dimensionless Group Reynolds number $\left(Re = \rho\bar{U}L/\eta_0\right)$ is introduced based on density ρ, characteristic velocity scale $\bar{U}$ (terminal velocity of the sphere) and length scale $L=a$ (sphere radius). From this, a time scale is derived $\left(L/\bar{U}\right)$, the inverse of which defines a characteristic deformation rate; together with the zero-shear rate viscosity $\left(\eta_0\right)$. Then, a solvent-fraction ratio may be defined as $\beta_{\text{solvent}} = \eta_{\text{solvent}} \big/ \left(\eta_{\text{solvent}} + \eta_{\text{polymeric}}\right)$, where η_{solvent} and $\eta_{\text{polymeric}}$ represent individual solvent and solute components, respectively.

2.1 Constitutive modelling: FENE-CR, Extensional White-Metzner FENE-CR models

Here one seeks a constitutive model that leads to a constant shear viscosity, and yet, possesses the specific rheometrical properties of relevance to Boger-type fluids, such as: a quadratic N_1 over a reasonable range of shear rates, giving way to some weakening; but also, vanishing N_2 (see Chilcott and Rallison [25]).

The FENE-CR model (Finite Extendible Nonlinear Elasticity - Chilcott and Rallison) satisfies these requirements and provides the following expression for the stress, expressed through a conformation transformation and a configuration tensor **A**, as:

$$Wi\,\overset{\nabla}{\mathbf{A}} + \mathrm{f}(\mathrm{Tr}(\mathbf{A}))(\mathbf{A} - \mathrm{I}) = 0. \tag{3}$$

Here, the stretch functional $\mathrm{f}(\mathrm{Tr}(\mathbf{A}))$ in eq. (3) depends on the trace (**A**) and the extensibility parameter L_{FENE}, and is given by:

$$\mathrm{f}(\mathrm{Tr}(\mathbf{A})) = \frac{1}{1 - \mathrm{Tr}(\mathbf{A})/L^2_{FENE}}. \tag{4}$$

Then, the extra-stress is recovered, in split form from the corresponding polymeric stress ($\boldsymbol{\tau}$) and solvent contribution, as

$$\boldsymbol{T} = \boldsymbol{\tau} + 2\beta_{\mathrm{solvent}}\mathbf{d},$$

where Kramers expression relates stress and configuration tensors, viz.

$$\boldsymbol{\tau} = \frac{(1-\beta_{\mathrm{solvent}})}{Wi}\mathrm{f}(\mathrm{Tr}(\mathbf{A}))\mathbf{A}. \tag{5}$$

Note here, use of the non-dimensional Group Weissenberg number, $Wi = \lambda_1 \bar{\mathrm{U}}/a$, with dependency upon a single relaxation time (λ_1) and a characteristic rate ($\bar{\mathrm{U}}/a$). Moreover, as discussed below in depth, note that incrementation in *Wi* may be gathered under elevation of characteristic rate (flow-rate, *Q*-increase; through rise in terminal flow velocity U), or under elevation of fluid elastic-memory (λ_1-increase). Accordingly, notation and equivalence in scaling used, between the experimental ($Wi^{\mathrm{Aber}}_{\lambda_1} = Wi^{Exp}_{\lambda_1} = \lambda_1 U/a$) and simulation ($Wi^{Swan}_{\lambda_1} = Wi^{Sim}_{\lambda_1} = \lambda_1 \bar{U}/L$) Weissenberg numbers is provided in Appendix-I.

Furthermore, a viscoelastic *extensional* White-Metzner model has also been investigated, combining the benefits of the White-Metzner formulation (White and Metzner [26]) with a viscous extensional model (as proposed by Debbaut & Crochet [30], Debbaut *et al.* [31], and used in Tamaddon-Jahromi *et al.* [32]). One notes that the White-Metzner model itself was derived from network theory applied to polymers. The theory assumes a flowing polymer consisting of long-chain molecules, connected in a continuously changing network structure with temporary junctions. Here, a modified White-Metzner constitutive equation has been introduced, in which the viscosity η becomes a function of the second and third generalised invariants of the rate-of-strain tensor [33]. As such, this equation is able to incorporate extensional-hardening effects within the expression for the viscosity (extension-rate dependency), without affecting the behavioural response in shear.

The resulting hybrid constitutive model is then a combination of the FENE-CR model with the extensional White-Metzner model, termed the swanINNFM model. This combination was inspired by our earlier trials and experiences with a similar hybrid construction of extensional White-Metzner with the linear-PTT model [32]. Such an swanINNFM model (see [33] for choice of naming convention) is expressed as:

$$T = \frac{(1-\beta_{\text{solvent}})}{Wi} \text{f}(\text{Tr}(\mathbf{A}))\mathbf{A}\phi(\dot{\varepsilon}) + 2\beta_{\text{solvent}}\phi(\dot{\varepsilon})\mathbf{d}, \quad (6)$$

where $\phi(\dot{\varepsilon})$ is defined below in expressions (7) and Appendix-II.

The Debbaut and Crochet [30] viscosity form [$\cosh(\lambda_D\dot{\varepsilon})$] is also incorporated here, in this swanINNFM version, introducing the extension-rate ($\dot{\varepsilon}$) and a dissipative material time-scale parameter of (λ_D):

$$\phi(\dot{\varepsilon}) = \cosh(\lambda_D\dot{\varepsilon}). \quad (7)$$

Alternative truncated forms of $\phi(\dot{\varepsilon})$ are provided in Tamaddon-Jahromi et al. [33] Appendix-II, in particular the quadratic form $\phi(\dot{\varepsilon}) \approx 1+(\lambda_D\dot{\varepsilon})^2$ (indicated swanINNFM(q)) strongly favoured in this work for its less-severe dissipative contribution with $(\lambda_D\dot{\varepsilon})$-rise.

The extensional viscosity of the new model is displayed in Fig. 1 for the range of $0.1 \le \lambda_D \le 1.5$. Here, an increasing trend in η_e is traceable for swanINNFM(q) model, in comparison against that for the FENE-CR model. Sharp increase in extensional viscosity is presented with the value of λ_D =1.5 around the strain-rate of $O(0.3)$. For lower value of λ_D =0.1 and λ_D =0.5, the extensional viscosity (η_e) for swanINNFM(q) model follows that of FENE-CR up to strain-rates of around $O(3)$ and $O(2)$, respectively.

Furthermore and in order to attain high-*Wi* solutions for the models discussed above, the following algorithmic modifications have been proven necessary.

ABS-f-correction. As demonstrated in [27] under thixotropic modelling, there are instances in mixed-type complex flow, as within the 4:1:4 contraction/expansion and near numerical *Wi*-solution breakdown, in which the dissipation function becomes negative, thus predicting negative values of the $f-$functional during flow evolution and along the spatial domain. To avoid this possibility arising, and whilst retaining consistency with the underlying ideal shear and extensional flow derivation theory, a corresponding modification to the FENE-CR configuration tensor model of eq. (4) has been proposed, of the form:

$$\text{f}(\text{Tr}(\mathbf{A})) = \frac{1}{1-\text{Tr}(|\mathbf{A}|)/\text{L}^2_{\text{FENE}}}. \quad (8)$$

Then, applying the absolute-value operation (ABS-correction to $\text{f}_{\text{FENE-CR}}$), to every constituent component of the trace function, has the desired effect of significantly boosting Wi_{crit}-levels (see [27] for more details).

Centreline shear-free boundary condition imposition – VGR-correction The symmetry flow centre-line is the unique region in the flow-domain of uniaxial extension. The velocity gradient recovery correction procedure (VGR-correction) prevents build up of spurious numerical noise in solution evolution, both throughout

the individual *Wi*-solution states, and subsequently, through successive continuation-stages of *Wi*-incrementation. Such VGR-correction is imposed solely on the centreline, enforcing: (i) shear-free flow, ensuring 1D-extensional deformation (eq. 9); (ii) the pure extensional uniaxial relationship between the normal deformation-gradients (eq. 10); and (iii) nodal-pointwise continuity imposed exactly, via a discrete approximation form (eq. 11). Adopting notation of $\hat{\dot{\varepsilon}} = \dfrac{\partial u_z}{\partial z}$ (as a function of *z*-spatial variable, in uniaxial extension along the flow centreline), for the extension-rate on the centreline in the axial direction, then the following identities may be established and imposed via VGR-correction:

$$\frac{\partial u_z}{\partial r} = \frac{\partial u_r}{\partial z} = 0, \tag{9}$$

$$\frac{\partial u_r}{\partial r} = -\frac{1}{2}\frac{\partial u_z}{\partial z} = -\frac{1}{2}\hat{\dot{\varepsilon}}, \tag{10}$$

$$\frac{u_r}{r} = -\left(\frac{\partial u_z}{\partial z} + \frac{\partial u_r}{\partial r}\right) = -\frac{1}{2}\hat{\dot{\varepsilon}}. \tag{11}$$

Note that, eq. 11 has been utilised throughout the domain (in the constitutive equation), irrespective of 1D-centreline arguments.

2.2 *Problem specification*

In this study and following the experimental data of Jones *et al.* [1], different sphere-to-tube radius ratios have been considered. Here, creeping flow is assumed ($Re \approx O(10^{-2})$) and as a result, the momentum convection term contribution is negligible. By default, the solvent contribution β_{solvent} is taken to be 0.9, which is compatible with the use of Boger fluids in the experiments. Typical time-steps employed are of the order $O(10^{-4})$ and a relative-increment time-stepping termination tolerance is selected (by default) of the order of 10^{-6} to determine temporal convergence to a steady state. Fig. 2 depicts the set of triangular meshes employed to satisfy solution spatial accuracy and mesh refinement requirements, showing zoomed sections around the sphere. In this study three specific meshes have been utilised, corresponding to the three geometric aspect-ratios of: a) $\beta_{\text{sphere}} = 0.5$, b) $\beta_{\text{sphere}} = 0.4$, and $\beta_{\text{sphere}} = 0.2$. To arrive at these choices, mesh refinement analysis has been covered elsewhere (Matallah *et al.* [33]). The number of degrees of freedom associated with these mesh are {35122, 42944, 51496} for $\beta_{\text{sphere}} = \{0.5, 0.4, 0.2\}$, as recorded in Table 1 along with other detailed characteristics for each mesh.

The drag force on the sphere may be represented through the integration of projected pressure and stress components over the sphere surface (governed by quadrant angle $0 \le \theta \le \pi$, in the flow plane, centred at sphere-centre), providing the dimensionless expression [16]

$$D = 2\pi a^2 \int_0^{\pi} \left\{ T_{rz} \sin(\theta) + (T_{zz} - p)\cos(\theta) \right\} \sin(\theta) d\theta. \tag{12}$$

As a consequence, the drag force, in an *unbounded Newtonian* fluid, is given by the so-called Stokes drag as $D_\infty = 6\pi\eta_0 a U_\infty$, where the sphere radius is (a=*L*), (η_0) is the fluid viscosity, and ($U_\infty = \mathrm{U}$) is the free-stream velocity far from the sphere. Then, the required drag coefficient in the bounded case is defined as $K = D / D_\infty$. With respect to calibration of Newtonian drag values, Happel and Brenner [22] presented typical wall-correction factors for rigid spheres moving in a still liquid in a cylindrical tube. In Table 2, these Newtonian drag values are summarized, covering the three geometric β_{sphere} ratios of current interest. In this data, excellent agreement is observed, when comparing our predicted drag values against those from the theory of Happel and Brenner [22].

3. Numerical discretisation

In the present work, the *hybrid finite element/finite volume* (*fe/fv) scheme* used is an extension of that previously cited in references Belblidia *et al*. [28]; Wapperom and Webster [35]; Webster *et al.* [36]. In essence, the numerical solution procedure adopts a time-stepping fractional-staged approach to steady-state, specifically developed and advanced for viscoelastic flow problems. It combines a Taylor series expansion in time for the convection-diffusion subproblem, with a time-incremental pressure-correction scheme for the generalised Navier-Stokes equations. This furnishes a semi-implicit scheme for incompressible flow, implemented over three sub-staged equations per time-step. Spatial discretisation is accomplished in part by the velocity-pressure finite-element approximation, on the parent-level quadratic-linear interpolation over the meshed-domain triangulation. This is accompanied by a cell-vertex stress finite-volume approximation on each triangular sub-cell of an individual parent-triangular cell. Thus, the incompressible momentum-continuity equations are discretized and solved through this hybrid combination of: semi-implicit Taylor-Galerkin/incremental pressure-correction algorithm (see, for example, Donea [37]; Zienkiewicz *et al.* [38]; Matallah *et al.* [39]), together with that of a cell-vertex finite volume sub-cell technique for stress.

Traditionally, finite volume methods have been devised to address conservation laws, for which it is convenient to segregate into term-types, along with their individual treatment, of flux, source and temporal derivative terms. For the flux terms arising, cell-vertex *fv*-schemes applied to the configuration-stress (**A**) equation are based upon a fluctuation distribution upwinding technique, which distributes control volume residuals to provide nodal solution updates. Fluctuation distribution (FD) schemes, originally designed for pure advection problems, have been devised to satisfy properties of conservation, linearity preservation and/or positivity: they appear in various forms, for example – minimum diffusion (low-diffusion) B-scheme (*LDB*); positive streamwise invariant (*PSI*) scheme (Wapperom and Webster [40]). Then, the configuration stress nodal-update over an *fv*-cell and a single time-step has two contributions per node – one from its fluctuation distribution component, and another from its uniform distribution component subtended by its median dual cell (unique per node, non-overlapping nearest neighbour region, one-third kite-area of its triangular *fv*-cell). This procedure demands appropriate area-weighting to maintain consistency in time, and for temporal accuracy reasons has been extended to time-terms likewise (see Webster *et al.* [36] for complete details). Being nodally-based, the VGR-correction procedures outlined above may be directly incorporated within the nodal *fv*-approximation for the configuration stress-variable solution components.

Such a hybrid-combined *fe/fv* scheme forms a time-stepping process, with a three fractional-staged structure and *pc*-formulation per time-step. On each time-step cycle $[t^n, t^{n+1}]$ commencing from $(\mathbf{u}, \mathbf{A}, p)^n$, the first stage solves a set of equations for velocity-stress update, subject to the current time-step pressure-solution (p^n) (and immediate-past time-step pressure-solution (p^{n-1}) for full incremental-*pc* form) in the momentum-stress equation subset. Second, the forward time-step pressure (p^{n+1}) is updated by imposing the continuity constraint through a Poisson equation on the temporal pressure-increment (p^{n+1}-p^n) (which may be suitably adjusted with a time-derivative of density for compressible flow (Keshtiban *et al.* [41]). At a third stage, the first fractional-stage velocity field ($\mathbf{u}^*$) is corrected with the updated pressure field temporal increment (p^{n+1}-p^n), to deliver the end-of-time step velocity field ($\mathbf{u}^{n+1}$). Fuller detail on these procedures is provided in the references cited above, together with Aboubacar et al. [42].

4. Experimental drag measurement

Jones *et al.* [1] described experiments on an isolated sphere of radius *a* falling under gravity in a bath of viscoelastic fluid. The experimental results correspond to two types of Boger fluids: Type-I based on a mixture of maltose syrup/water-based with 0.1% PAA (polyacrylamide) and Type-II containing a 0.19% PIB w/v (polyisobutylene) with a solvent consisting of polybutene (93%) and 2-chloropropane (7%). The rheological properties show that both types of fluids exhibited constant shear viscosity, over a sensible range of shear-rates, giving way to some slight shear-thinning at high shear-rates. Equally, it is reported that first normal stress-difference (N_1) results show the classical quadratic behaviour.

Two separated experimental devices were employed for each of the two types of Boger fluids. The first experimental set-up consisted of a rectangular cross-section (10cm x 5cm) and length of 80cm. The second one consisted of perspex cylindrical tubes with varying diameters in the range of 12, 6 and 2.13 cm. In a similar manner, spheres of different radii and densities were used. In the same study experimental results were reported for three aspect-ratios, the benchmark tight-fitting case $\beta_{\text{sphere}} = 0.5$, medium-fit $\beta_{\text{sphere}} = 0.4$, and the wide-fit case $\beta_{\text{sphere}} = 0.2$ (approximating unbounded). Type-I Boger fluids showed enhanced drag for $\beta_{\text{sphere}} = 0.25$. However, this enhancement essentially disappeared for the more tight-fitting instance of $\beta_{\text{sphere}} = 0.5$, where within experimental error, findings could be considered as Newtonian in response,.

The experimental data for Type-I Boger fluids in the limiting case $\beta_{\text{sphere}} \to 1$ and against a comparable Newtonian fluid (of the same zero shear-rate viscosity), clearly showed a substantially lower sphere-velocity, indicating significant drag enhancement. Even though the available data for the maltose syrup-based Boger fluids was limited, the findings indicated that a turning-point was likely in drag-coefficient (K/K_N) response whilst varying β_{sphere} (drag enhancement claimed with $\beta_{\text{sphere}} = 0.25$, less in evidence for $\beta_{\text{sphere}} = 0.5$).

A series of experiments for Type-II Boger fluid was conducted - one after mixing (newly mixed liquid Type-II(i)) and another after a pause of some two months, spanning a period of ~eight months (aged liquid Type-II(ii)). On this basis, an interpolation curve-fitting procedure was employed to yield the respective isobeta curves, where error bars are appropriate, both in terms of the fitting and the raw data measurements. Nevertheless, such data are held as a sound indicator of (K/K_N)-levels and general trends in drag response. The authors admitted that the data gathered with these two Boger fluids has shown some distinctive differences, and may be argued to be associated with the time taken by the polyisobutylene chains to achieve their equilibrium configuration in the viscous polybutene solvent.

Furthermore, some drag reduction in the experimental data for Type-II(i) fluid was observed at low *Wi*, followed by large enhanced drag at higher *Wi*. Comparably, there was no drag reduction found with Type-II(ii) fluid; clearly different behaviour between the two sets of data for the same fluid. Experimental results on the aged-sample (Type-II(ii)) showed that within experimental error, (K/K_N, *Wi*) data in the range $0 \leq \beta_{\text{sphere}} \leq 0.15$ are independent of β_{sphere}. There appears to be a minor increment in (K/K_N)-values at fixed *Wi* in the range $0.15 < \beta_{\text{sphere}} \leq 0.2$. Fig. 3 reproduces the three isobeta (K/K_N, *Wi*) curves reported in Jones *et al.* [1] for β_{sphere}={0.2, 0.4, 0.5} and the Type-II(i) Boger fluid. Values of β_{sphere} near 0.2 would appear to provide the maxima in drag-coefficient. For values in the range $0.2 < \beta_{\text{sphere}} \leq 0.5$, there is substantial decline in drag-coefficient values at any fixed *Wi*, as concluded for Type-I fluids. The benchmark-case corresponding to the fitted-case $\beta_{\text{sphere}} = 0.5$, shows some initial decrease in K/K_N to *Wi*~0.3, beyond which drag enhancement is reported. Subsequently, a critical solution level is reached at *Wi*=1.35 with K/K_N =1.3. Regarding the medium-fit $\beta_{\text{sphere}} = 0.4$ instance, there is only a slight indication of initial drag-reduction at low *Wi*, prior to reaching *Wi*~0.15, followed by more rapid drag enhancement (than for $\beta_{\text{sphere}} = 0.5$ case) to Wi_{crit}=1.30. Finally, in the wide-fitting case $\beta_{\text{sphere}} = 0.2$, there is barely any initial drag-reduction captured in the interpolation, as found in the more-fitted instances. However, it must be acknowledged here, that only two data-points are taken, at mid-to-larger rates. Hence, there is insufficient information at low rates to determine more precisely the position on early drag undershoot. For this particular $\beta_{\text{sphere}} = 0.2$ instance, the final and maximal drag-value reached is K/K_N=2, corresponding to *Wi*=1.30.

5. Prior evidence from numerical solutions

Effect of normal stress (N_1) and extensional viscosity (η_e) on drag: Models A-D, α, J, and FENE-CR models - earlier results

Much of the initial development and background work to the present study is covered in Aguayo *et al.* [42]. There, the work focussed on the Oldroyd-B model and only on enhanced pressure-drop measurement, whilst addressing contraction and contraction-expansion type-flows, under both planar and axisymmetric configurations. As a follow on, in Tamaddon-Jahromi *et al.* [17] various numerical studies were performed on drag enhancement for the (2:1) flow-past-a-sphere problem, alongside pressure-drop enhancement for the (4:1:4) contraction-expansion flow problem. In this manner,

it was possible to compare and contrast the similarities in nature of these two classical flow problems. The main objective there was to shed light on the key material functions that were responsible for such enhancements, in both drag and pressure-drop.

In order to achieve this particular goal, Tamaddon-Jahromi *et al.* [24] compared and contrasted drag response for four *constant shear-viscosity* models (designated A-D), each incrementally adjusting a single material functional property from its base-Newtonian (A-model) form (constant η_e, vanishing N_1, no memory). This provided material functions for three representative model-variants (B-D) (see Tables 1 and 2 in Tamaddon-Jahromi *et al.* [33]) - a purely-viscous extensional-inelastic form (B-model; non-zero η_e, vanishing N_1, no memory); a White-Metzner C-model (constant η_e, non-zero N_1, with memory); and the classical Oldroyd-B form (D-model; non-zero η_e, non-zero N_1, with memory). The lack of finite-extensibility of the Oldroyd-B model (D-model), and its over-strong sustained quadratic response in N_1, are both features overcome in subsequent work by drawing upon FENE-CR functionality (see below).

Over these four model variants, the corresponding drag predictions of [17], as reproduced in Fig. 4 against Wi^{sim}, were held to be highly instructive. For example, from this evidence it was apparent that the extensional-inelastic B-model was capable of generating the much-sought after experimental drag enhancement, resulting in a rapid rise within the low Weissenberg number range ($Wi<0.5$). Such a response could then be associated unequivocally with η_e-properties (when taken against A-Newtonian and D-Oldroyd comparatives). Nevertheless, early numerical instability set in with the B-model, beyond this relatively low *Wi*-stage. In contrast with the White-Metzner C-model (N_1-effects inclusion), an opposing and declining trend in drag was produced, this becoming gradually more pronounced with *Wi*-rise; prior to reaching a minimum in normalised *drag coefficient* (K/K_N) (value ~0.86) around Wi=1.2, and a steady-solution limit-point around Wi~1.3. Drag predictions with the designated D-model of Oldroyd-B form (frequently used to represent Boger fluid response), that comprised of both $\{\eta_e, N_1\}$-effects, gave an intermediate response between models B and C. Such findings revealed drag-reduction characteristics associated with N_1-effects (shared with model-C), whilst also indicating some retardation in the level of drag-reduction - an influence of η_e-effects (shared with model-B). Drag reduction for the D-model was fairly linear to Wi~0.8, then more pronounced in the range $0.8<Wi<1.0$, prior to flattening out to a minimum in drag coefficient (value ~0.92), with its steady limit-point at Wi~1.1. Hence, D-model basically replicates a hindered C-model response, slightly retarded and elevated in drag response.

In addition, still further exploration on drag response through more extensive constitutive variations, then drew upon *FENE-CR derivations*, as considered in Tamaddon-Jahromi *et al.* [17]. This development both permitted finite extensibility to be introduced and some weakening of N_1–properties, whilst retaining the prevailing constant shear viscosity favoured option. The N_1 behaviour for four such associated constitutive models is shown in Fig. 5a, with counterpart η_e-behaviour exposed in Fig. 5b. The η_e-properties show common unbounded response for Oldroyd-B, J-

model and α-model (see below), and elevation in hardening for FENE-CR with rising L_{FENE}. The Oldroyd-B N_1-form displays the classical strong quadratic N_1–response against *Wi*-rise, whilst the FENE-CR is weaker than this, but stronger than linear response. A third White-Metzner/J-model, introducing an additional constant J-parameter in N_1–functionality $(1+J(\dot{\gamma}^m)$, m=2), flattens the N_1–response within the rate decade $10^0 \leq Wi \leq 10^1$. Still, a fourth White-Metzner/α-model has been found useful too, which introduces an additional constant α-parameter on the *Wi*-convective term of the constitutive model. Amongst other things, this has the effect of lateral shifts across the rate decades (retarding mechanism) in N_1–functionality (note, α-model in Table 3). Then, combined and hybrid model FENE-CR(αJ^m)-forms are also included, to reflect more generalised master-constructs with J-model, α-model and FENE-CR combinations. This allows one to explore alternative slopes in N_1–functionality, between zeroth and second-order, achieved by varying rate exponent m-parameter, in the range $\{0.1 \leq m \leq 0.5\}$. At the same time, delayed and damped response may be introduced into N_1–response, via lateral rate-shifts with an α-parameter of 0.1.

Tamaddon-Jahromi *et al.* [17] provided much of the drag data in Fig. 6 to represent a range of results for individual J-model, α-model, D-model and FENE-CR, alongside the theoretical prediction with the master-model generalisation of FENE-CR(αJ^m). From this further evidence, one can gather the positive enhanced-drag results available under both J-model and α-model realisations. The *pure FENE-CR form*, with both L_{FENE}={3, 5} extensibility-parameter setting, effectively demonstrates that the unbounded extensional viscosity of D-model may be overcome. The Oldroyd-B D-model has its early *Wi* steady-limit ~1.1 attaining a drag of 0.916. Nevertheless, FENE-CR provides for only O(2%) drag-reduction, plateauing to drag levels of {K/K_N =0.97, L_{FENE}=3}, {K/K_N =0.96, L_{FENE}=5} at considerably larger *Wi* levels above 500 (actual limitation ~$O(10^b)$, b=3). The slightly larger limiting drag observed for L_{FENE}=3 above L_{FENE}=5, may be attributed to the weaker form for $N_1(L_{FENE}=3)$ than that for $N_1(L_{FENE}=5)$, which dominates any differences due to η_e-elevation, between η_e (L_{FENE}=3) and η_e (L_{FENE}=5).

The J-model construct suffers from the rather severe limitation of low *Wi*-attenuation for steady solutions, and even more so than for the classical Oldroyd-B, D-model (with which it shares common extensional viscosity form, hence lacking in finite extensibility). This is held to be a further consequence of the functional complexity of the J-model. The J-model(J=1.0) only reached the solution limit-point of *Wi*=0.5, corresponding to a drag of K/K_N =1.05; with J-model(J=0.1) the limit-point is also *Wi*=0.5, and the corresponding drag-value is K/K_N ~1.002. The *enhanced-drag response* with the α-model of O(10%) for *Wi*=5.8, provides the most encouragement, both in terms of drag-enhancement level and extended range of *Wi*-solution attainment. This α-model result follows modest drag reduction up to *Wi*~4.0 (note, the similarity in trend here to some experimental findings).
It is on this basis that the master model-generalisation FENE-CR(αJ^m) was proposed, targeting the combination of J-model and α-model drag-enhancement, whilst coupling this to high-elasticity capability of the FENE-CR model. Hence, the theoretically derived drag-curve for FENE-CR(αJ^m), which was anticipated to reach elasticity levels one order larger, *Wi*~$O(10^2)$ and drag-enhancement of O(100%). Unfortunately, in practice, such a FENE-CR(αJ^m)-version inherits similar numerical

convergence characteristics to those of the J-model, and hence presents a barrier to further progression along this path.

The way forward here is chartered by earlier findings and successes in modelling enhanced pressure-drops in contraction flows [32]. There, a hydrid constitutive model was proposed, from the combination of the viscous Debbaut and Crochet model [30] (with the extensional viscosity functionality) and the viscoelastic Linear Phan-Thien-Tanner (LPTT) model. The Debbaut and Crochet [30] and Debbau *et al.* [31] papers offered the inclusion of a dissipative [$\cosh\left(\lambda_D \dot{\varepsilon}\right)$] viscosity-law form, to provide an extensional viscous representation which unaffects that in shear. In [31], this particular hybrid combination of eWM_LPTT was conceived of as an extensional-viscosity White-Metzner type model, layered on top of the LPTT model(β_{solvent}=0.9); hence, with minimal shear-thinning impact. There, comparison was performed on enhanced pressure-drops (*epd*) between this viscoelastic eWM_LPTT and its equivalent purely-viscous extensional model, which in the viscous context, naturally gave rise to consideration of flow-rate increase (*Q*-increase, see below) to increment through deformation-rate (natural protocol to experimental practice). Such an eWM_LPTT supplied for the first time, some hope in capturing experimental-levels of enhanced pressure-drops in contraction-expansion flows over the relevant deformation-rate range (Rothstein and McKinley [44]). It is on this basis that the LPTT model has been replaced with a FENE-CR form, providing the counterpart eWM_FENE-CR, here renamed simply as swanINNFM model (as in section 2), following the constant viscosity line of investigation pursued thus far. The earlier constitutive model derivations that relied upon sub-functionals of $\{\phi_1, \phi_2, \phi_3\}$ to dictate $\{\eta_e, N_1\}$-formalisation, may also be re-applied here, but now adopting ϕ_2 of cosh-form (or its truncated quadratic-expansion equivalent), and setting $\phi_1 = \phi_3 = 1$(see Tables 1 and 2 in Tamaddon-Jahromi *et al.* [33]). Then, a stress-tensor framework provides the necessary steps to derive an equivalent swanINNFM structure. Additional benefit is then taken of the FENE-CR configuration-tensor (A-variable) construction, so that the dissipative contributions lie within the Kramers-stress reconstruction from the configuration-tensor, and hence, lie outside the differential evolution equation for the viscoelastic components of the system (*a benefit that proves of some numerical advantage*). To aid more-ready comparison, a schematic summary of the constitutive models cited above is provided in Table 3, along with their corresponding material properties and drag predictions.

6. Present simulation results versus experimental evidence: various geometric ratios, flow-rate (*Q*-increase)

Here, numerical solutions with the *proposed new hybrid model of* swanINNFM(q) are contrasted against the experimental drag data of Jones *et al.* [1], focusing on the three specific geometry aspect-ratios, β_{sphere}={0.2, 0.4, 0.5}. The following analysis adopts standard experimental procedure for the falling-sphere problem, when considering *increasing terminal sphere-velocity with the same fluid* (through size/mass adjustment of the sphere) and hence, affecting an increase in flow rate (*Q*). Experimentally and at fixed geometric-ratio of $\beta_{\text{sphere}} = 0.5$, as in Jones *et al.* [1], this implies incrementation through sphere and tube-radii, and hence, providing data on the various ratios, governed by sphere (*a*) to tube (*R*) radii ($\beta_{\text{sphere}} = a / R$).

6.1 Drag predictions with $\beta_{\text{sphere}} = 0.5$

First, for this particular benchmark geometry choice, the normalised *drag coefficient* (K/K_N) is plotted in Fig. 7 against $Wi_{\lambda_1}^{Exp}$, with solutions extracted at each incremental value of λ_D, selected at intervals between $0 \le \lambda_D \le 0.55$, spanning the experimental data. In the first instance with $\lambda_D = 0$, the drag coefficient is simply that previously reported [17] with the original FENE-CR(L_{FENE}=5) model, providing the base comparison. Subsequent and consecutive positive incrementation in λ_D, is noted to stimulate a pronounced impact on drag. This is a direct consequence of increased dissipative contributions to the constitutive model (private communication, M.H. Wagner; see Tamaddon-Jahromi *et al.* [33]). Though in this instance the experimental data points are sparse (*see on*), the rise in drag is clearly now evident, and the family of λ_D–solutions provide a tight window of capture of $0.25 \le \lambda_D \le 0.45$ for this data. In particular, this finding identifies the close match for the (λ_D=0.35)-solution. Beyond the experimental-data point at $Wi_{\lambda_1}^{Aber}$=1.35, steady solutions become more difficult to establish, and a relatively short phase is entered of oscillatory solutions (up to Wi_{crit}=1.9, see on). In this phase, further steady solutions may only be extracted upon reduction in the λ_D–level, to say λ_D=0.3 as shown (switch of notation symbols). A *first upper-limit* in drag coefficient of K/K_N ~1.35, applies when numerical solutions become unsteady (*first transition point*). This limit is depicted with a dashed horizontal line, and would appear to apply across a wide range of flow-rates (see cross-symbols for corresponding λ_D). The subsequent oscillatory phase occurs prior to meeting a *second upper-limit* in drag coefficient, where *divergence* is encountered. Here, temporal instability is detected, as noted in progressively sampled pressure solution values (under $Wi_{\lambda_1}^{Exp}$ rise) - first steady, then oscillatory, finally numerically divergent – when the solution becomes finally intractable, with rapid divergence in the time-stepping process.

Flow oscillation and temporal instability. To further analyse the temporal limiting drag position, Fig. 8 presents the results on comparative sampled-pressure just above the sphere (location indicated; (r, z) = (1.7, 0.0), in vertical plane of sphere-origin), in terms of evolutionary data for ever rising *Wi*-solutions at $\lambda_D = 0.35$. In this form, the temporal variation of pressure is presented, whilst covering the solution interval *Wi*=[0.4, 1.9]. In passing, one notes that there is barely any indication of counterpart temporal fluctuations in the velocity field. From this evidence, one can detect - the initial onset of temporal oscillation in the interval $1.3 < Wi \le 1.4$, its continued growth with *Wi*-rise in oscillation amplitude (fixed frequency), to the high-pressure oscillatory state at *Wi*=1.9 (between pressure-levels, 40 to 60 units). Beyond $Wi_{crit} = 1.9$ solution state, numerical divergence is encountered and the problem becomes intractable henceforth.

Solution fields Corresponding pressure, first normal stress difference (N_1) fields and stress components profiles at the symmetry line are presented in Fig. 9 at $\lambda_D = 0.35$ for various $Wi_{\lambda_1}^{Exp}$ ={0.4, 1.3, 1.5, 1.9}. The pressure fields of Fig. 9A, shown in 2D and 3D perspective, reveal solution increments pre-sphere that eventually cover the

whole sphere region as *Wi* rises. Solutions for ($Wi \leq 1.3$) are steady; solutions for ($Wi \geq 1.4$) are oscillatory-unsteady. *Pressure maxima* (at upstream stagnation point, see 3D form) increase by some seven-times, from $Wi=0.4$ to $Wi=1.9$. It is interesting to note that the low-pressure region, aft of the sphere, becomes larger, and detaches upon approaching the critical solution level of $Wi_{crit}=1.9$ (divergent subsequently). Furthermore, the area of low-pressure around the sphere significantly reduces at the oscillatory state of $Wi=1.5$, when compared with the steady-state solution at $Wi=1.3$. Representative pressure minima at $Wi=1.5$ reach -6.4 units, whilst they approach -17.5 units at $Wi=1.3$, see Fig. 9A. In Fig. 9B, there is further evidence, where equivalent first normal stress difference (N_1) solutions become larger, aft-sphere (higher strain rates in the wake region), whilst a region of low N_1 prevails pre-sphere (low strain rates). Here, first normal stress maxima around the sphere, increase by some 4.6 times from $Wi=0.4$ to $Wi=1.3$ and by 1.6 times from $Wi=1.3$ to $Wi=1.9$. The locations of N_1 minimums and maximums are clearly visible from the 3D plots of Fig. 9B. Here, large values of N_1 above the sphere stretch over the sphere wake-region as *Wi* increases. Moreover, a region of N_1-minimum develops in front of the sphere with *Wi* rise (almost 14 times increase in N_1-minimum from $Wi=0.4$ to $Wi=1.9$, as of -1.2 units to -16.5 units). In addition, and as observed at $Wi=0.4$ in Fig. 7, the drag value lies under the Newtonian reference line. At this position, Fig 9A displays a N_1-maxima of 4.2 units above the sphere. With $Wi=1.3$, the maximum N_1-values (19.3 units) increase by almost four-times in comparison to $Wi=0.4$, showing a significant drag enhancement of $K/K_N=1.2$. Likewise at $Wi=0.4$, the development of high stress in the wake region is shown, with a maximum of $N_1=13.7$ units, contrasting against the maximum value of 2.1 units in the same region at $Wi=0.3$. Note also that, the largest value of symmetry-line N_1 increases by almost 11 times from $Wi=0.4$ to $Wi=1.9$ (from $N_1=0.5$ unit to 5.7 units).

Some interesting features can be elucidated from Fig. 9C where profiles of stress components are observed along the symmetry line and around the sphere for $Wi_{\lambda_1}^{Exp}=\{0.4, 1.3, 1.5, 1.9\}$. As anticipated, the maximum normal stresses (τ_{zz}, τ_{rr}) values on the sphere surface and in the wake region are observed to grow with *Wi*. This explains the origin of the enhanced drag shown at high *Wi* ($Wi>0.4$) in Fig. 7. Here and as *Wi* rises, the shear-stress (τ_{rz}) exhibits increasingly positive and negative values around the sphere. The values of the third azimuthal component of normal stress ($\tau_{\theta\theta}$), observed at centreline and along the sphere, are insignificant in comparison to axial (τ_{zz}) and radial (τ_{rr}) stress components.

6.2 Predictions with $\beta_{\text{sphere}} = 0.4$

The medium-fit aspect-ratio of (Fig. 10) shows further enhancement in experimental drag calculations (now three-data points provided, with undershoot for $Wi_{\lambda_1}^{Exp}<0.25$, from the interpolation) above that for $\beta_{\text{sphere}} = 0.5$. This new aspect-ratio setting demands still larger levels of λ_D-parameter, in order to match predictions with this refreshed set of experimental data. Typically here, the drag coefficient reaches the larger level of $K/K_N \sim 1.7$ at $Wi_{\lambda_1}^{Exp}=1.25$. This has led to trialling simulations with $0.35 \leq \lambda_D \leq 0.62$, which has provided a wide span of predictive data, and a tighter window of capture for the experimental data with $0.45 \leq \lambda_D \leq 0.62$. Anticipating error bars on the experimental data, across the three aspect-ratios provided, one can gather

from the simulation fits that (λ_D =0.55)-solution matches both the lower and mid-range data-points, but undershoots the upper data-point. In contrast, the (λ_D =0.62)-solution matches both lower and upper-data point, but overshoots the mid-range data-point. Interpolation across the original experimental data of Jones *et al.* [1] for the three aspect-ratios within the mid-point range, would indicate that this experimental mid-data-point measurement is subject to a larger error-bar. One suspects that this measurement should lie more closely to (λ_D =0.62)-curve (as for other β_{sphere}-factors). In this medium-fit instance of $\beta_{\text{sphere}} = 0.4$, the *steady-unsteady first-transition* dashed-line becomes located around K/K_N ~1.73, somewhat above that of K/K_N ~1.35 for the $\beta_{\text{sphere}} = 0.5$ case. In this more severe testing circumstance for $\beta_{\text{sphere}} = 0.4$, and to retain steady solutions up to the larger drag threshold demanded here, it has been necessary to halve the time-step factor (lowering temporal discretisation error, adjusting convergence tolerance threshold accordingly) for solutions beyond a prior limit-line at K/K_N ~1.31 (as indicated). To further support the $\beta_{\text{sphere}} = 0.4$ drag evidence and to detect the transition from *steady-unsteady* solutions with rising-*Wi*, again attention may be directed to study the evolution of the sampled-pressure above the sphere for the characteristic value of λ_D =0.45. Here, it is evident from Fig. 11 that such sampling becomes unsteady, and subject to oscillations of growing amplitude, within the interval $1.8 \leq Wi \leq 2.1$, with onset prominent by *Wi*=1.9 (note, somewhat delayed from the reported onset of oscillation at *Wi*=1.4 for the earlier tighter-fit case ($\beta_{\text{sphere}} = 0.5$, λ_D =0.35), shown in Fig. 8). Once more, beyond this terminating solution stage numerical divergence ensues; hence in this instance, Wi_{crit} is 2.1.

6.3 Predictions with $\beta_{\text{sphere}} = 0.2$

The wide-fitting, less-constrained aspect-ratio corresponding to $\beta_{\text{sphere}} = 0.2$ (Fig. 12), has proven to be the most severe test-case to resolve numerically, with maximum experimental drag coefficient measured of K/K_N ~2.0. This case highlights only two experimental data points, in the mid-to-upper rate-range. The appropriate trial range of λ_D-values in the simulations is now located as $0.25 \leq \lambda_D \leq 0.75$, which reveals a modest drag undershoot at low values of $Wi \leq 0.2$ (not shown in the original experimental data fits), and enhanced drag subsequently at larger *Wi*. The severity of the problem now demands additional strategies to secure steady solution states, beyond the dashed drag-threshold line indicated. For this problem instance, a direct flow-rate increase continuation strategy gave immediate numerical divergence in the time-stepping beyond this dashed-drag threshold line, at each value of λ_D attempted. To progress further for each λ_D –value, a successful continuation strategy used was then to freeze the flow-rate setting (indicated with vertical arrows at selected flow-rate values, equivalent to fixing $Wi_{\lambda 1}^{Exp}$), and conduct continuation through λ_D –rise. This procedure was cross-checked under solutions with other geometry aspect-ratios to confirm consistency in drag calculation, irrespective of continuation option (λ_D – rise or rate-rise). In this manner, the experimental data [1] was well-captured with $0.63 \leq \lambda_D \leq 0.65$, inclusive of the upper rate-range drag data-point. Undoubtedly, the increased severity of the problem with its excessive drag levels, makes this aspect-ratio the most challenging to resolve, both experimentally and through simulation. A

comparative summary of the various drag-data extracted is supplied through Fig. 13 and Table 4 across each geometric aspect-ratio trialled. This covers the key experimental drag measurements used, against their counterpart predictions under variable dissipative time-scale of λ_D ($0.35 \le \lambda_D \le 0.62$).

7. Fluid parameter λ_1 - increase and solvent-fraction variation

7.1 Flow-rate (Q-increase) vs λ_1-increase flow conditions

Figure 14 compares and contrasts the two modal-approaches to defining the flow problem for analysis – through increasing fluid relaxation-time (same terminal velocity for different fluids, common preference under simulation) and increasing problem flow-rate (through the terminal velocity, retaining the same fluid, preferred option under experimentation). Here and initially, base-settings apply of geometric ratio ($\beta_{\text{sphere}} = 0.5$) and solvent fraction ($\beta_{\text{solvent}} = 0.9$). As such Fig. 14a reflects drag findings for *Wi*-increase through fluid-elasticity (λ_1 *-increase*, charted against $Wi_{\lambda_1}^{Exp}$ definition). Relative comparison is also made against FENE-CR and α–model solutions, where the evidence of null drag response for FENE-CR (slight drag reduction) is apparent over a wide range of *Wi*, and modest but delayed drag enhancement is detected with the α–model (more dissipative). To capture the experimental data under this λ_1*-increase* solution-mode, it is necessary to continually increment the λ_D -value, alongside *Wi*-incrementation (through λ_1), so that $0.75 \le \lambda_D \le 1.39$. In fact, a cubic relationship may be established between λ_D and λ_1; a fact that illustrates the complex interplay between dissipative time-constant and the fluid relaxation time at fixed terminal velocity. Nevertheless, on the positive side and in contrast to FENE-CR and *α*–model findings, a close fit to the experimental data is practical, with the proviso of the amplified levels of λ_D necessary in order to satisfy this goal.

The corresponding and contrasting position under increasing terminal velocity is exposed within Fig. 14b (*Q*-increase). Under this continuation procedure in *Wi*, a close match to the experimental data is realised with a *single dissipative fluid time-constant* of $\lambda_D = 0.35$, up to *Wi*=1.35. Particularly creditable is the fine capture of the final upper-rate experimental data-point and the close tracking with the predictions of the experimental interpolation curve (based on only two data-points). Beyond this stage, a reduced value of λ_D =0.3 is necessary to sustain steady solutions (as indicated with the dashed-line). As discussed above, oscillatory solutions in the pressure field are detected above K/K_N=1.3, around when $Wi_{\lambda_1}^{Exp} = 1.4$. One concludes from this evidence, the *importance of selection of the same procedure* of *Wi*-continuation across experimental and computational protocols, if one is to derive sensible and comparable levels of drag.

Clearly the λ_1 *-increase* mode, is somewhat more protracted than the *Q*-increase mode, and as such, less robust as a reliable method for accurate drag prediction and enhanced drag capture.

7.2 Influence of β_{solvent} on Drag

Having identified the position above for $\beta_{\text{solvent}} = 0.9$ and Boger-fluid composition, it is also instructive for past-reference to the literature, to identify what impact the above deliberations have whilst considering alternative solvent-fraction composition. To do this, the drag coefficient is considered for three values of solvent-fraction, β_{solvent} = {0.9, 0.5, 1/9}, and for the two protocols of *Wi*-incrementation – increasing fluid relaxation-time at fixed terminal velocity (λ_1-*increase*, Fig. 15a), and increasing terminal velocity at fixed fluid relaxation-time (*Q*-increase, Fig.14b). This covers fluid composition with high-solvent ($\beta_{\text{solvent}} = 0.9$), to high-solute ($\beta_{\text{solvent}} = 1/9$), passing through the intermediate stage for ($\beta_{\text{solvent}} = 0.5$). In this comparison exercise, the default geometry aspect-ratio used is β_{sphere}=0.5 and the dissipative time-constant is $\lambda_D = 0.25$. Results with the base FENE-CR model are also included for direct cross-reference.

The overview position from Fig. 14a,b is such that drag enhancement is only accessible via *Q-increase*; hence, this is absent from λ_1-*increase* results of Fig. 15a, a finding consistent with the literature (as for Oldroyd-B model predictions [17]). Under *Q*-increase alone of Fig.14b, the high-solute ($\beta_{\text{solvent}} = 1/9$)-data again imparts no drag enhancement (monotonically declining), prior to a relatively early termination of steady solutions around *Wi*~1.15. A more complete picture of trends with still larger *Wi* is provided through ($\beta_{\text{solvent}} = 0.5$)-data. Here, the early monotonic decline is succeeded by reaching a lower minimum at *Wi*~0.7, with subsequent upturn, and intercepting the Newtonian reference line at *Wi*~2.3. The limit for steady solutions is reached at *Wi*~2.6, which represents a modest level of 5% drag enhancement. This trend-pattern for $\beta_{\text{solvent}} = 0.5$ stands alone in its clear depiction of the local minimum and the transition from drag suppression-to-enhancement (reminiscent of Oldroyd-B results – and pressure-drop findings in [17]; and drag computations for flow-past-a-cylinder in Owens & Phillips [13]). Final steady-solution limit-points vary between solvent-fractions, with elevation to 25% drag enhancement at *Wi*~1.9 and $\beta_{\text{solvent}} = 0.9$ (crossing Newtonian drag-line at *Wi*=0.75), for the same level of dissipative time-constant $\lambda_D = 0.25$. By raising the dissipative time-constant to $\lambda_D = 0.35$ (as shown in Fig.14b), drag is enhanced further to 30% (K/K_N =1.3), whilst the *Wi*-steady-limit drops still further to *Wi*~1.5. At $\beta_{\text{solvent}} = 0.9$, there is evidence, though only slight, of early initial drag-reduction to a local minimum restricted to the zone $Wi \leq 0.4$.

In contrast, the counterpart data with λ_1-*increase* of Fig.15a, displays *only drag-reduction* with *Wi*–rise and at each set β_{solvent}-value; though once more, one may note that drag does increase with elevation of β_{solvent}. Under this context of relatively static deformation-setting, limiting trends at larger-*Wi* tend to asymptote to a constant level of drag, and steady *Wi* limit-points are considerably larger than under *Q*-increase (see Table 5; *a new challenge to reproduce for the experimental community*). These critical steady *Wi* limit-points are reported as *Wi*={1.1, 2.6, 1.9} for β_{solvent}={1/9, 0.5, 0.9}. Drag findings with high-solvent $\beta_{\text{solvent}} = 0.9$, are practically replicated between those for the base-FENE-CR model and the new eWM_FENE-CR($\lambda_D = 0.35$) model.

One notes in passing and in contrast to the above, this is because of the relatively low setting of the dissipative time-constant, which is shown above to require some elevation (to $0.75 \leq \lambda_D \leq 1.39$) in order to reflect drag enhancement.

8. Conclusions

A detailed study of the *drag* characteristics in flow-past-a-sphere has revealed some encouraging and provocative results. A new model with an extension-rate dependent viscosity White-Metzner/FENE-CR model (swanINNFM) has proven itself well-capable of capturing the levels of enhanced drag, previously observed in experimental measurements, and impressively, over comparable measures of deformation-rates. New algorithmic steps have proven necessary to provide this match and the required increase in Wi_{crit}. These steps include using: i) absolute *f*-functional representation (*ABS-f*-correction); ii) centreline velocity-gradient correction (VGR-correction); iii) continuity correction; iv) conformation tensor-**A** problem definition; v) flow-rate increase, as opposed to fluid-relaxation time increase.

In this work, three geometric ratios of $\beta_{\text{sphere}} = 0.5$, $\beta_{\text{sphere}} = 0.4$, and $\beta_{\text{sphere}} = 0.2$ have been closely analysed to derive a match to the experimental drag data of Jones *et al.* for their fluid Type-II [1]. Primarily, and for a single geometric aspect-ratio ($\beta_{\text{sphere}} = 0.5$), solution parametric windows have been predicted that encapsulate the available experimental data. *In itself, such tight-capture is believed to be a significant and novel computational breakthrough,* albeit under a single-mode Maxwell relaxation-time approximation and steady-state conditions. We cite Tamaddon-Jahromi *et al.* [33] with respect to discussion on the *modelling of Boger fluids,* and the use of a more representative multi-mode approximation, for its impact on present *drag (or epd)*-findings. It must be conceded that multi-mode approximation may tighten this position up somewhat further (whilst retaining the use of dissipative I_D–factor), through improved fitting to experimental fluid properties over wider deformation-rate ranges, though what is particularly sought here is better matching to steady extensional-viscosity (not that in shear-viscosity alone). Tamaddon-Jahromi *et al.* [33] also provides fuller discussion on the *derivation of a physical understanding to this new* swanINNFM *model* (with extension-rate dependent viscosity, constant in shear – hence, extensional dissipative response), applicable across length-scales and coordinate reference (considering fibre suspension additives).

Subsequently, this position is then extended to alternative length-scales, with more loosely-fitting aspect-ratios of $\beta_{\text{sphere}} = 0.25$ and 0.2, where similar realisation is gathered. Here, and for smaller β_{sphere} values, larger λ_D values are required to match the experimental measurements. Furthermore, a new mode of flow instability has been identified with *Wi*-rise from the instantaneous pressure data. For β_{sphere}=0.5 with $\lambda_D = 0.35$, oscillatory fluctuations in pressure sample-point data above the sphere appear at *Wi*=1.4. This oscillatory phase survives up to *Wi*=1.9, prior to eventually giving way to an unstable divergent state. This position adjusts for the aspect-ratio of β_{sphere}=0.4, where pressure oscillation is observed at *Wi*=1.8 with λ_D=0.45.

A main realisation in this study is the *importance of selecting the same procedure* of *Wi*-continuation across experimental and computational protocols, if one is to derive sensible and comparable levels of drag. Clearly the λ_1 *-increase* mode, is more protracted than the *Q*-increase mode, and as such, less robust as a reliable method for accurate drag prediction. It is also observed that flow-rate increase (*Q-increase*) conditions show larger drag enhancement, when compared to fluid-relaxation time increase (λ_1*-increase*), at the same level of λ_D.

Finally, numerical solutions with adjustment in fluid solvent-fraction (β_{solvent}=0.9, 0.5, 1/9) have also been considered, in one particular geometric aspect-ratio instance ($\beta_{\text{sphere}} = 0.5$). Here, only (*Q-increase*) solutions are found to yield drag enhancement; counterpart (λ_1 *-increase*) solutions only provide drag reduction (as reported frequently in the computational literature). At any specific fixed elasticity level, there is an increase in drag observed with rise in β_{solvent}. The results with the high-solute/low-solvent composition of β_{solvent}=1/9 (and relatively low-dissipative base-factor of λ_D=0.25), only showed a declining trend in drag, largely in agreement with the literature (in which λ_D=0).

Acknowledgement
Sincere thanks must be expressed to the many helpful contributions made to this study through our colleagues in the INNFM Wales, but particularly to Professor Ken Walters FRS. I.E. Garduño gratefully acknowledges financial support from Consejo Nacional de Ciencia y Tecnología (Mexico) through the scholarship No. 310618.

Dedication
This work has been written and dedicated to the memory of a dear sister-in-law, Linda Webster, recently deceased.

Appendix I*: Group Weissenberg numbers: Experimental versus Numerical*

Based on a sphere radius (a cm) and extracted characteristic velocity (from flow-rate and terminal velocity identity) of U cm/s, standard experimental practice would provide for incrementation in an experimental Weissenberg number ($Wi_{\lambda_1}^{\text{Aber}} = Wi_{\lambda_1}^{Exp} = \lambda_1 \text{U}/a$) through raising U/a at fixed fluid relaxation time, λ_1. Experimentally, this approach proves convenient for retention of the same fluid across multiple flow-rate test runs (*Q*-increase). One notes that the value reported in the experimental studies of Jones *et al.* for the relaxation time of Boger fluid Type-II is $\lambda_1 = 0.38$ s.

Equivalently, in the simulations, a Weissenberg number ($Wi_{\lambda_1}^{Swan} = Wi_{\lambda_1}^{Sim} = \lambda_1 \bar{U}/L$) is often stipulated, where $\bar{\text{U}}$ is a characteristic velocity (terminal velocity of the sphere) and L is a characteristic length (taken here as the radius of the sphere). In this form, common practice is to increment the simulation Weissenberg number ($Wi_{\lambda_1}^{Swan} = \lambda_1 \bar{U}/L$) by raising the fluid relaxation time, λ_1, at fixed rate, U/a (λ_1-*increase*). Computationally, this choice is convenient as it renders common inlet boundary condition imposition over the respective differential problems – effectively holding flow-rate fixed (base levels of deformation), whilst varying the relaxation time in the stress equation (varying the fluid).

One may derive a relationship between these two definitions of Weissenberg number, experimental ($Wi_{\lambda_1}^{\text{Aber}} = \lambda_1 \text{U}/a$) and computational ($Wi_{\lambda_1}^{Swan} = \lambda_1 \bar{U}/L$), and hence establish a scaling factor, in order to compare experimental and simulation findings on a one-to-one basis.

From Jones *et al.* and assuming an experimental sphere radius of $a = 0.635$ cm, and a fluid relaxation time of $\lambda_1^{exp} = 0.38$ s, identifies:

$$Wi_{\lambda_1}^{Aber} = \lambda_1 \frac{U}{a} = 0.38\left(\frac{U}{0.635}\right).$$

From which, for example and to *identify a base value of unity* in the Group number $Wi_{\lambda_1}^{Aber}$, provides for a terminal velocity of U =1.67cm/s and a rate of $\frac{\text{U}}{a} = \frac{1.67}{0.635} = 2.63 \text{ s}^{-1}$.

Following similar lines of argument for the *Wi*-simulation definition, and noting that the rate-factor $\left(\bar{U}/L\right)$ is held fixed (which may be taken unambiguously as base-factor of unity s^{-1}), whilst varying (λ_1), then:

$$Wi_{\lambda_1}^{Swan} = \lambda_1 \frac{\bar{U}}{L} = \lambda_1 .$$

As such, unity may also be established for $Wi_{\lambda_1}^{Swan}$ with a relaxation time setting of $\lambda_1^{sim} = 1$ s.

On this basis, one may establish parity in common Group numbers, when one recognises the fixed factor in each definition: $\left(\bar{U}/L\right)$ =1s^{-1} in the simulations, $\lambda_1^{exp} = 0.38$ s in the experiments. Hence, a scaling factor of $(1/\lambda_1^{exp})$ emerges, which yields:

$Wi_{\lambda_1}^{Swan} = 2.63 Wi_{\lambda_1}^{\text{Aber}}$.

Subsequently, once base parity has been established, the actual method of *Wi*-incrementation employed, experimentally of computationally, is of course open to selection in either setting.

References

[1] W. Jones, A. Price, K. Walters, The motion of a sphere falling under gravity in a constant-viscosity elastic liquid, J. Non-Newton Fluid Mech. 53 (1994) 175–196.

[2] K. Walters, R.I. Tanner, The Motion of a Sphere Through an Elastic Fluid, in: R.P. Chhabra, D. De Kee (Eds.), Transport Processes in Bubbles, Drops and Particles, Taylor & Francis, New York, 1992: pp. 73–86.

[3] R.A. Brown, G.H. McKinley, Report on the VIIIth international workshop on numerical methods in viscoelastic flows, J. Non-Newton Fluid Mech. 52 (1994) 407–413.

[4] G.H. McKinley, Steady and Transient Motion of Spherical Particles in Viscoelastic Liquids, in: D. De Kee, R.P. Chhabra (Eds.), Transport Processes in Bubbles, Drops and Particles, 2nd ed., Taylor & Francis, New York, (2002) pp. 338–375.

[5] B. Caswell, O. Manero, B. Mena, Recent developments on the slow viscoelastic flow past spheres and bubbles, Rheology Reviews (2004) 197–223.

[6] R.P. Chhabra, Bubbles, Drops, and Particles in Non-Newtonian Fluids, 2nd ed., CRC Press, Boca Raton, Fl, 2007.

[7] L.E. Becker, G.H. McKinley, H.K. Rasmussen, O. Hassager, The unsteady motion of a sphere in a viscoelastic fluid, J. Rheol. 38 (1994) 377–403.

[8] R. B. Bird, R. C. Armstrong, O. Hassager, Dynamics of Polymeric Liquids Vol 2 (Wiley, New York), 1987

[9] M. Solomon, S. Muller, Flow past a sphere in polystyrene-based Boger fluids: the effect on the drag coefficient of finite extensibility, solvent quality and polymer molecular weight, J. Non-Newton Fluid Mech. 62 (1996) 81–94.

[10] G. Tiefenbruck, L.G. Leal, A numerical study of the motion of a viscoelastic fluid past rigid spheres and spherical bubbles, J. Non-Newton Fluid Mech. 10 (1982) 115–155.

[11] B. Gervang, A.R. Davies, T.N. Phillips, On the simulation of viscoelastic flow past a sphere using spectral methods, J. Non-Newton Fluid Mech. 44 (1992) 281–306.

[12] B. Mena, O. Manero, L.G. Leal, The influence of rheological properties on the slow flow past spheres, J. Non-Newton Fluid Mech. 26 (1987) 247–275.

[13] R.G. Owens, T.N. Phillips, Steady viscoelastic flow past a sphere using spectral elements, Int. J. for Numer. Meth. in Eng. 39 (1996) 1517–1534.

[14] R.I. Tanner, Engineering Rheology, 2nd ed., OUP Oxford, Oxford, 2000.

[15] R.G. Owens, T.N. Phillips, Computational Rheology, Imperial College Press, 2002.

[16] J.V. Satrape, M.J. Crochet, Numerical simulation of the motion of a sphere in a Boger fluid, J. Non-Newtonian Fluid Mech. 55 (1994) 91–111.

[17] H.R. Tamaddon-Jahromi, M.F. Webster, P.R. Williams, Excess pressure drop and drag calculations for strain-hardening fluids with mild shear-thinning: Contraction and falling sphere problems, J. Non-Newton Fluid Mech. 166 (2011) 939–950.

[18] C. Bodart, M.J. Crochet, The time-dependent flow of a viscoelastic fluid around a sphere, J. Non-Newtonian Fluid Mech. 54 (1994) 303–329.

[19] W.J. Lunsmann, L. Genieser, R.C. Armstrong, R.A. Brown, Finite element analysis of steady viscoelastic flow around a sphere in a tube: calculations

with constant viscosity models, J. Non-Newton Fluid Mech. 48 (1993) 63–99.
[20] Y.R. Fan, R.I. Tanner, N. Phan-Thien, Galerkin/least-square finite-element methods for steady viscoelastic flows, J. Non-Newton Fluid Mech. 84 (1999) 233–256.
[21] J. Happel, H. Brenner, Low Reynolds number hydrodynamics: with special applications to particulate media, First, Martinus Nijhoff Pub, The Hague, 1983.
[22] R. Zheng, N. Phan-Thien, R.I. Tanner, On the flow past a sphere in a cylindrical tube: limiting Weissenberg number, J. Non-Newton Fluid Mech. 36 (1990) 27–49.
[23] J. Petera, A new finite element scheme using the Lagrangian framework for simulation of viscoelastic fluid flows, J. Non-Newton Fluid Mech. 103 (2002) 1–43.
[24] H.R. Tamaddon-Jahromi, M.F. Webster, K. Walters, Predicting numerically the large increases in extra pressure drop when boger fluids flow through axisymmetric contractions, J. Natural. Science. 2 (2010) 1–11.
[25] M. Chilcott, J. Rallison, Creeping flow of dilute polymer solutions past cylinders and spheres, J. Non-Newton Fluid Mech. 29 (1988) 381–432.
[26] J.L. White, A.B. Metzner, Development of constitutive equations for polymeric melts and solutions, J. Appl. Polym. Sci. 7 (1963) 1867–1889.
[27] J.E. López-Aguilar, M.F. Webster, H.R. Tamaddon-Jahromi, O. Manero, High-Weissenberg predictions for micellar fluids in contraction–expansion flows, J. Non-Newton Fluid Mech. 222 (2015) 190–208.
[28] F. Belblidia, H. Matallah, B. Puangkird, M.F. Webster, Alternative subcell discretisations for viscoelastic flow: Stress interpolation, J. Non-Newton Fluid Mech. 146 (2007) 59–78.
[29] F. Belblidia, H. Matallah, M.F. Webster, Alternative subcell discretisations for viscoelastic flow: Velocity-gradient approximation, J. Non-Newton Fluid Mech. 151 (2008) 69–88.
[30] B. Debbaut, M.J. Crochet, Extensional Effects in Complex Flows, J. Non-Newton Fluid Mech. 30 (1988) 169–184.
[31] B. Debbaut, M.J. Crochet, H.A. Barnes, K. Walters, Extensional effects in inelastic liquids, in: Xth Inter. Congress on Rheology, Australian Society of Rheology, Sydney, 1988: pp. 291–293.
[32] H.R. Tamaddon-Jahromi, F.S. Syed, M.F. Webster, Studies on Contraction Flows and Pressure-Drops-Extensional Viscosity and Dissipative Stress Effects, in: XVth International Congress on Rheology, AIP, Monterey, CA, 2008: pp. 225–227.
[33] H.R.Tamaddon-Jahromi, I.E. Garduño, J.E. López-Aguilar, and M.F. Webster, Predicting Excess pressure drop (*epd*) for Boger fluids in expansion-contraction flow, 2016, *in press* J. Non-Newton Fluid Mech.
[34] H. Matallah, P. Nithiarasu, M.F. Webster, Stabilisation Techniques for Viscoelastic Flows, in: ECCOMAS Computational Fluid Dynamics Conference, Swansea, 2001: pp. 1–19.
[35] P. Wapperom, M.F. Webster, A second-order hybrid finite-element/volume method for viscoelastic flows, J. Non-Newton Fluid Mech. 79 (1998) 405–431.
[36] M.F. Webster, H.R. Tamaddon-Jahromi, M. Aboubacar, Time-dependent algorithms for viscoelastic flow: Finite element/volume schemes, Numerical Methods for Partial Differential Equations. 21 (2005) 272–296.

[37] J. Donea, A Taylor-Galerkin Method for Convective-Transport Problems, International Journal for Numerical Methods in Engineering. 20 (1984) 101–119.

[38] O.C. Zienkiewicz, K. Morgan, J. Peraire, M. Vandati, R. Löhner, Finite Elements for Compressible Gas Flow and Similar Systems, in: 7th Int. Conf. Comput. Meth. Appl. Sci. Eng, Versailles, France, 2015.

[39] H. Matallah, P. Townsend, M.F. Webster, Recovery and stress-splitting schemes for viscoelastic flows, J. Non-Newtonian Fluid Mech. 75 (1998) 139–166.

[40] P. Wapperom, M.F. Webster, Simulation for viscoelastic flow by a finite volume/element method, Comput. Methods Appl. Mech. Engrg. (1999) 281–304.

[41] I. Keshtiban, F. Belblidia, M.F. Webster, Numerical simulation of compressible viscoelastic liquids, 122 (2004) 131–146.

[42] M. Aboubacar, H. Matallah, M.F. Webster, Highly elastic solutions for Oldroyd-B and Phan-Thien/Tanner fluids with a finite volume/element method: planar contraction flows, J. Non-Newton Fluid Mech. 103 (2002) 65–103.

[43] J.P. Aguayo, H.R. Tamaddon-Jahromi, M.F. Webster, Excess pressure-drop estimation in contraction and expansion flows for constant shear-viscosity, extension strain-hardening fluids, J. Non-Newton Fluid Mech. 153 (2008) 157–176.

[44] J.P. Rothstein, G.H. McKinley, The axisymmetric contraction–expansion: the role of extensional rheology on vortex growth dynamics and the enhanced pressure drop, J. Non-Newton Fluid Mech. 98 (2001) 33–63.

Table 1. Mesh characteristics: different sphere aspect ratios, $\beta_{\text{sphere}}=a/R=0.5$ (coarse, medium, refined), $\beta_{\text{sphere}}=0.4$, $\beta_{\text{sphere}}=0.2$

Meshes	Elements	Nodes	Degree of freedom $(\mathbf{u}, \tau, p)$	
$\beta_{\text{sphere}}=0.5$	1600	3381	21177	*coarse*
	2687	5610	35122	*medium*
	7400	15191	95042	*refined*
$\beta_{\text{sphere}}=0.4$	3306	6861	42944	
$\beta_{\text{sphere}}=0.2$	3986	8229	51496	

Table 2. Newtonian drag values (K_N): theoretical vs numerical (present study)

$\beta_{\text{sphere}}=a/R$	K_N Theory [20]	K_N numerical (present study)
0.2	1.680	1.688
0.4	3.596	3.592
0.5	5.970	5.931

Table 3. Constitutive models, material properties and *drag coefficients* (K/K_N), $\beta_{\text{sphere}}=0.5$

Models	**Material properties**	**β_{Solvent}**	**Critical *Wi* (Wi_{Crit})**	**(K/K_N) at Wi_{Crit}**
B-model (Generalised Newtonian)	η_e same as Old-B; η_s const; $N_1=0$	0.9	0.4	1.15
C-model (White- Metzner)	**(η_e , η_s) const; N_1 - damping**	0.9	1.3	0.86
D-model (Oldroyd-B)	η_e extreme strain hardening; η_s const; **N_1=quadratic**	0.9 0.5 1/9	1.1 1.0 1.2	0.94 0.86 0.69
α-model (White- Metzner)	**η_e** same as Old-B; η_s const; **N1=weaker than Old-B**	0.9	(α=0.1) 5.9	1.11
J-model (White-Metzner)	η_e same as Old-B; η_s const; **N_1 - damping (J=0, Oldroyd-B)**	0.9 0.9	(J=1.0) 0.5 (J=0.1) 0.5	1.02 0.99
FENE-CR(L=5)	η_e same as Old-B (capped); η_s const; **N_1 - damping**	0.9	O(500)	0.96

Table 4. Normalised *drag coefficient* (K/K_N), swanINNFM(q) model, experimental data vs predictions, variable λ_D, β_{sphere} =0.5, 0.4, 0.2, $\beta_{Solvent} = 0.9$

Model	β_{sphere}	**Wi**	**(K/K_N)** ***Prediction***	**(K/K_N)** ***Experimental***
swanINNFM(q) **λ_D =0.35**	0.5	0.49 3.48	0.956 1.241	0.944 1.250
swanINNFM(q) **λ_D =0.62**	0.4	0.65 2.25 3.35	1.004 1.278 1.570	1.012 1.258 1.672
swanINNFM(q) **λ_D =0.65**	0.2	2.1 3.5	1.481 2.041	1.484 2.009

Table 5 Critical Wi^{Exp} (Wi^{Sim}) and drag coefficient K/K_N, swanINNFM(q) model, solvent-fraction variation, λ_D =0.25

	λ_1-increase Wi^{Sim} (Wi^{Exp}) K/K_N	**Q-increase** Wi^{Sim} (Wi^{Exp}) K/K_N
$\beta_{solvent}$ =1/9	4.0 (1.5) 0.62	3.0 (1.1) 0.65
$\beta_{solvent}$ =0.5	55.0 (21.0) 0.78	7.0 (2.6) 1.02
$\beta_{solvent}$ =0.9	30.0 (11.0) 0.97	5.0 (1.9) 1.20

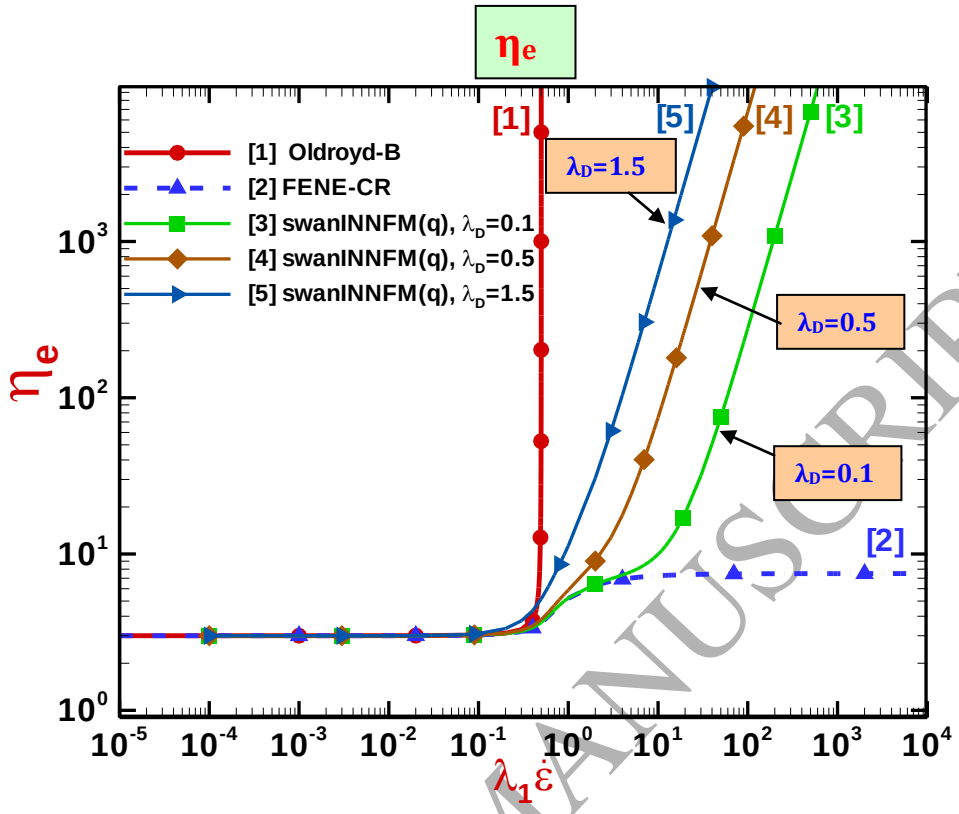

Fig. 1. Extensional viscosity of Oldroyd-B, FENE-CR, swanINNFM [$q\{1+(\lambda_D\dot{\varepsilon})^2\}$] models, $\lambda_D = 0.1,\ 0.5,\ 1.5,\ \beta_{solvent}$ =0.9

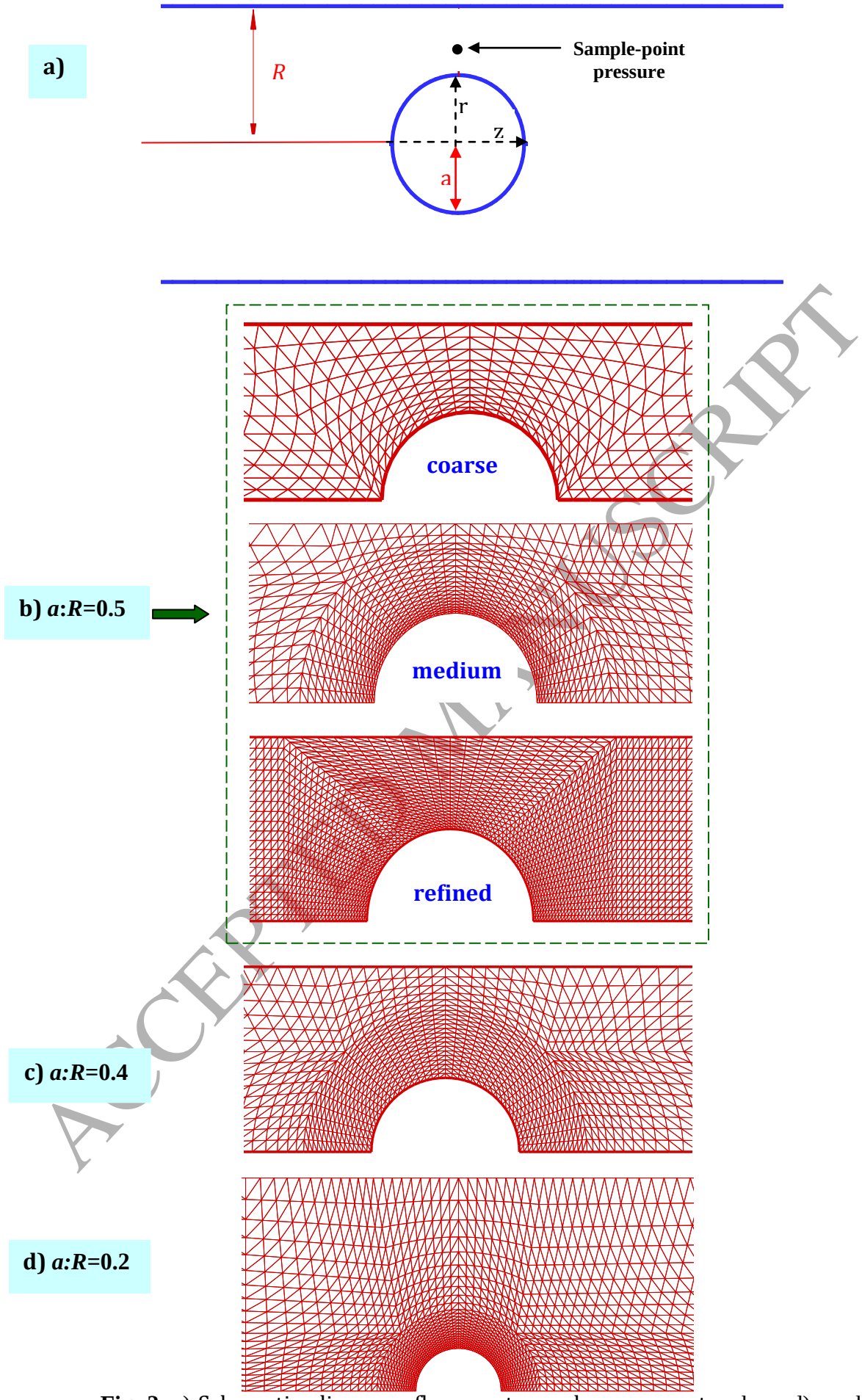

Fig. 2. a) Schematic diagram, flow past a sphere geometry; b, c, d) mesh patterns around sphere: b) β_{sphere} =a/R=0.5, coarse (*elts=1600, nodes=3381, dof=21177,*), medium (*elts=2687, nodes=5610, dof=35122*), and refined (*elts=7400, nodes=15191, dof=95042*); c) β_{sphere} =0.4; d) β_{sphere} =0.2

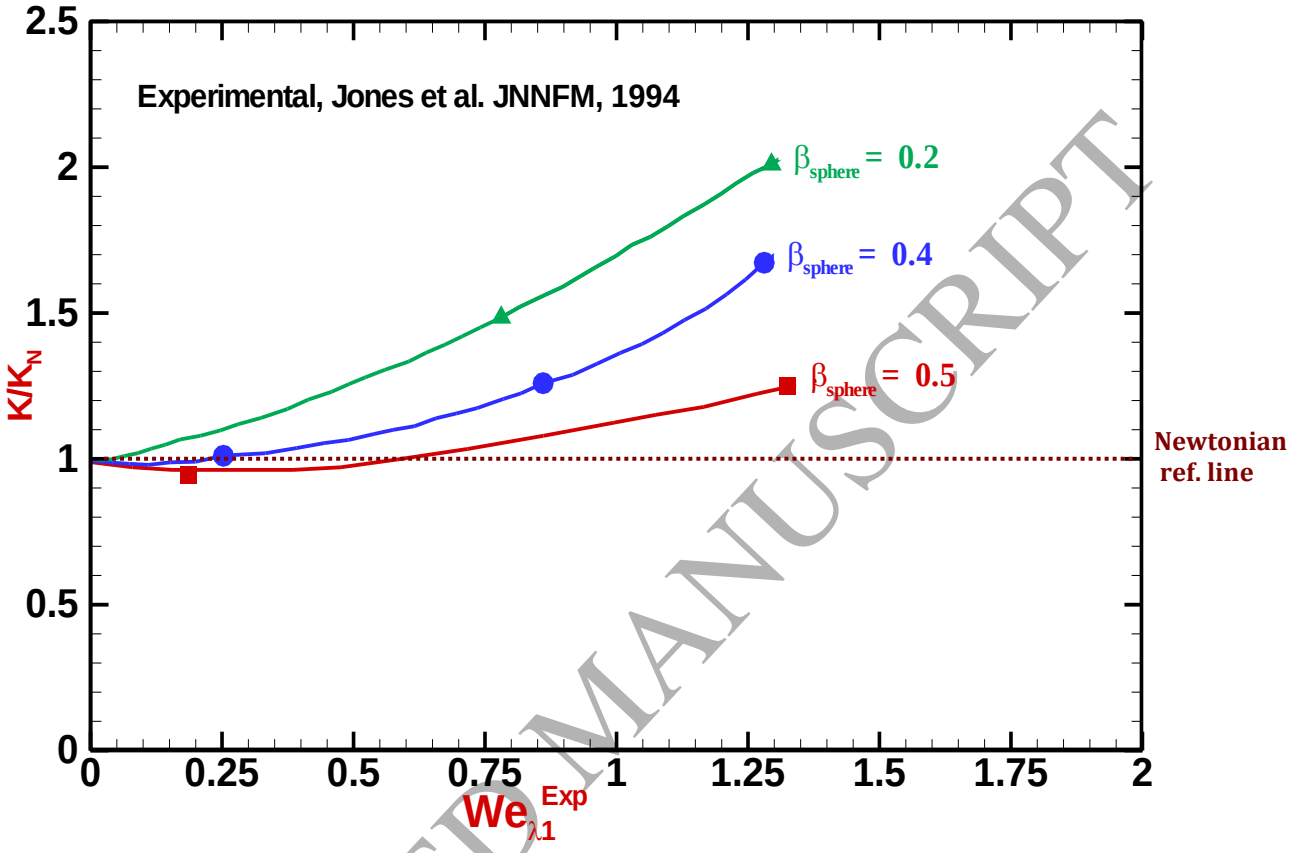

Fig. 3. Normalised experimental data (*drag coefficient* (K/K_N)) for Boger fluid Type-II(i) with different aspect ratios (β_{sphere} =a/R=0.5, 0.4, 0.2), Jones *et al.* [1]

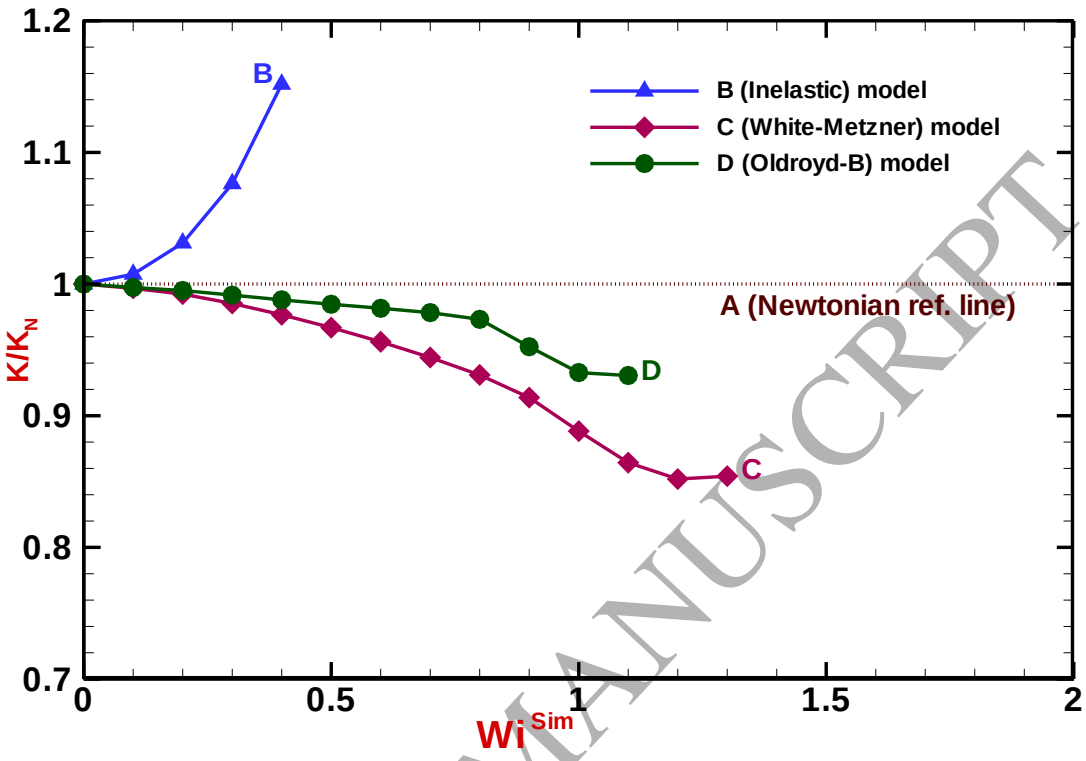

Fig. 4. Normalised *drag coefficient* (K/K_n) vs Wi^{Sim} for Inelastic (B), Oldroyd-B (D), and White-Metzner (C) models, $\beta_{solvent}$ =0.9, β_{sphere} =0.5

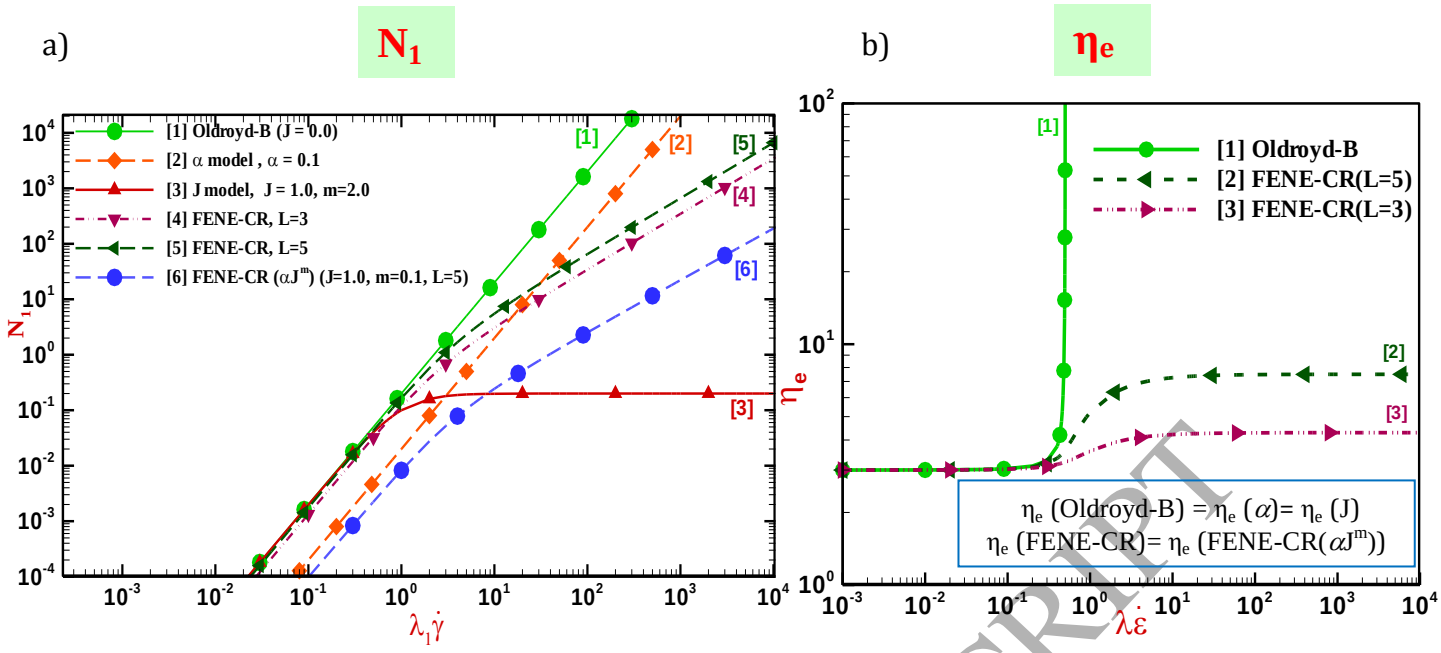

Fig. 5. Material function, a) first normal stress difference (N_1), b) Extensional viscosity (η_e): Oldroyd-B, α, J, FENE-CR, and FENE-CR(αJ^m) models

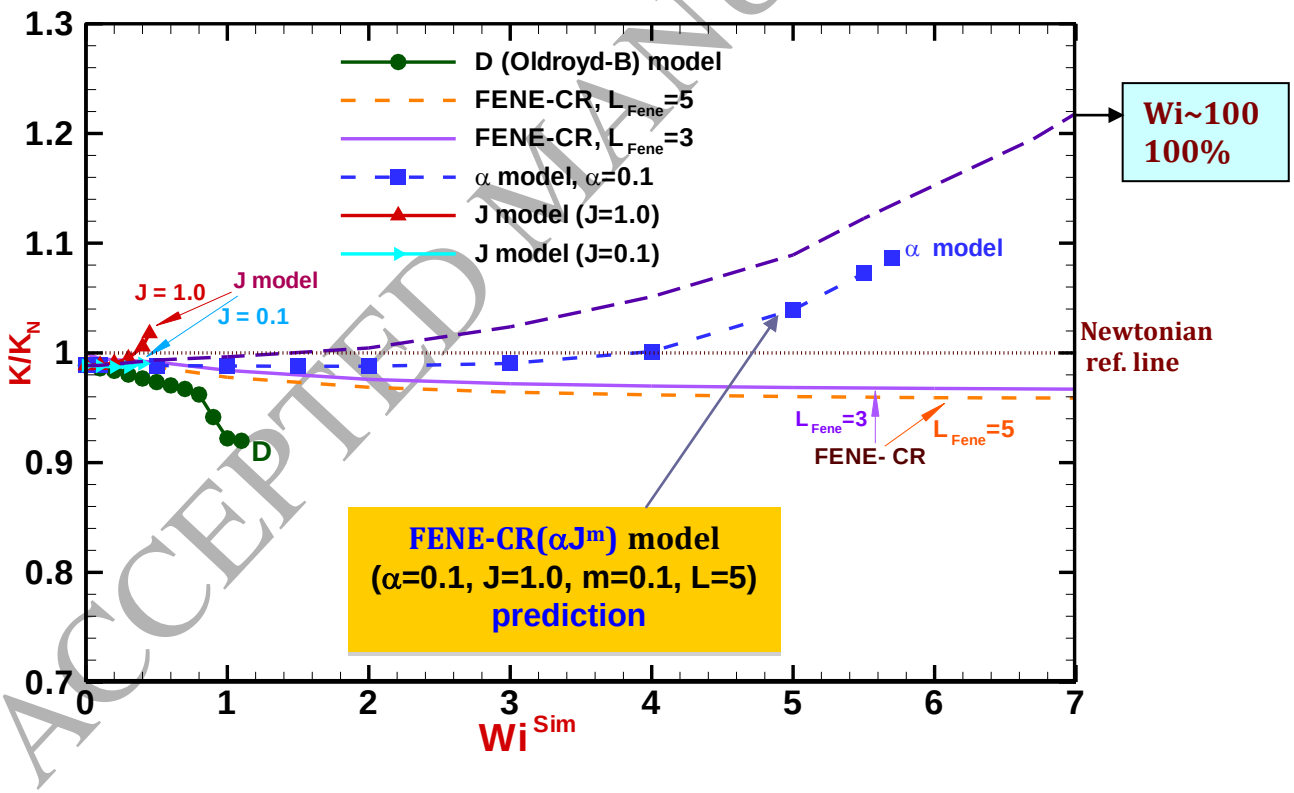

Fig. 6. Normalised *drag coefficient* (K/K_n) vs Wi^{Sim} for Oldroyd-B, J, FENE-CR, and FENE-CR(αJ^m) models, β_{sphere}=0.5

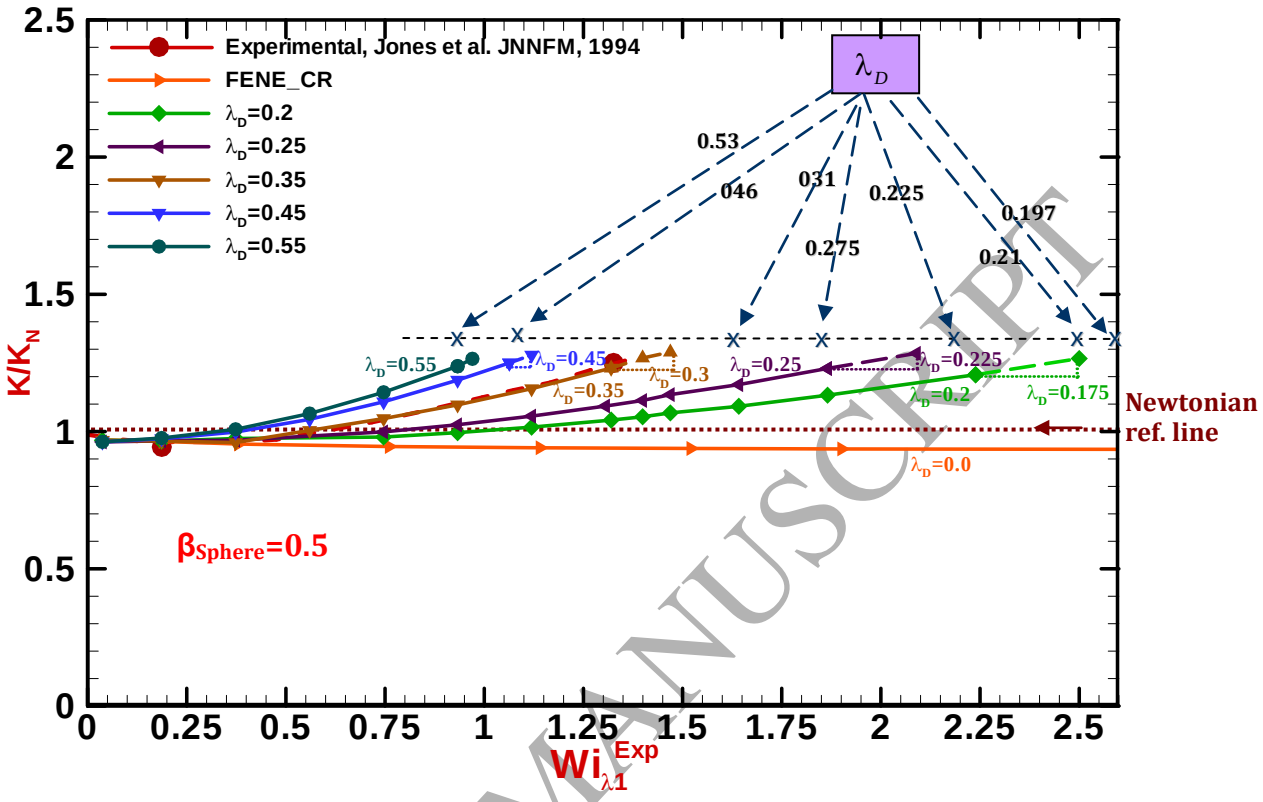

Fig. 7. Normalised *drag coefficient* (K/K_n) vs $Wi_{\lambda 1}^{Exp}$ for swanINNFM(q) model, L_{FENE} =5, $0 \leq \lambda_D \leq 0.55$, β_{sphere} =0.5

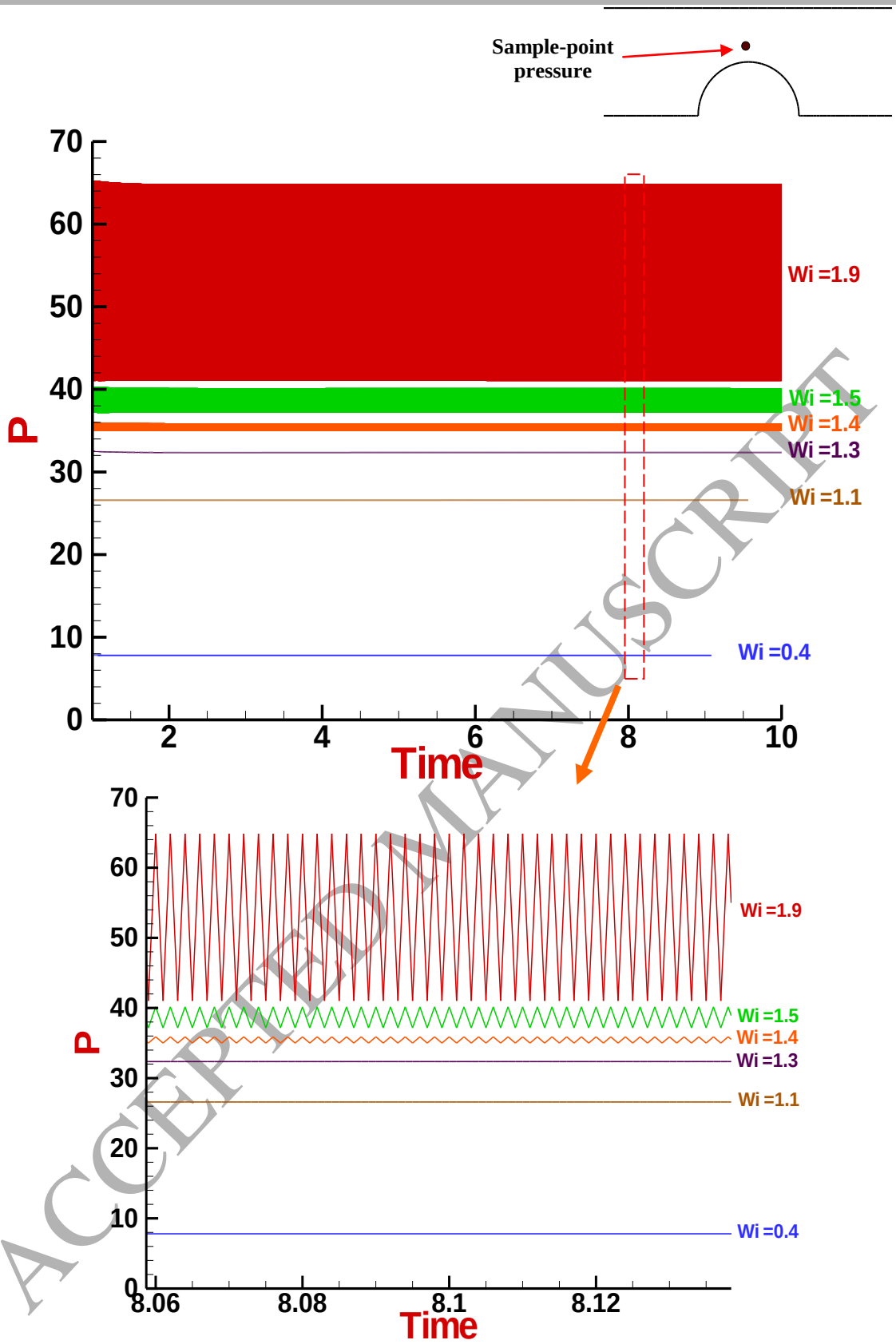

Fig. 8. Sample-point pressure evolution above sphere (as shown), various Wi^{Exp}, swanINNFM(q), Q-increase, $\lambda_D = 0.35$, $\beta_{\text{sphere}} = 0.5$

Fig. 9A

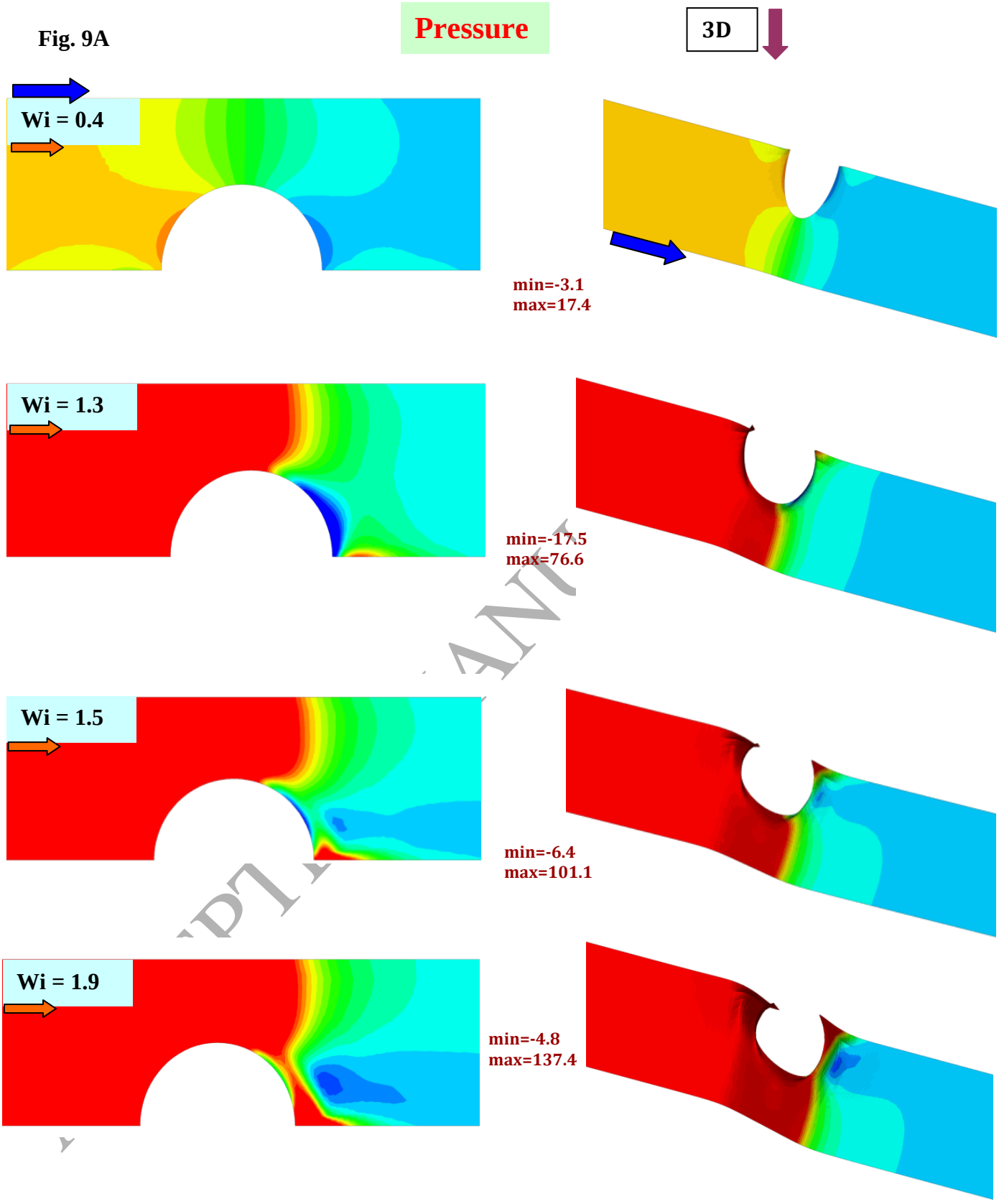
Pressure
3D
Wi = 0.4
min=-3.1
max=17.4
Wi = 1.3
min=-17.5
max=76.6
Wi = 1.5
min=-6.4
max=101.1
Wi = 1.9
min=-4.8
max=137.4

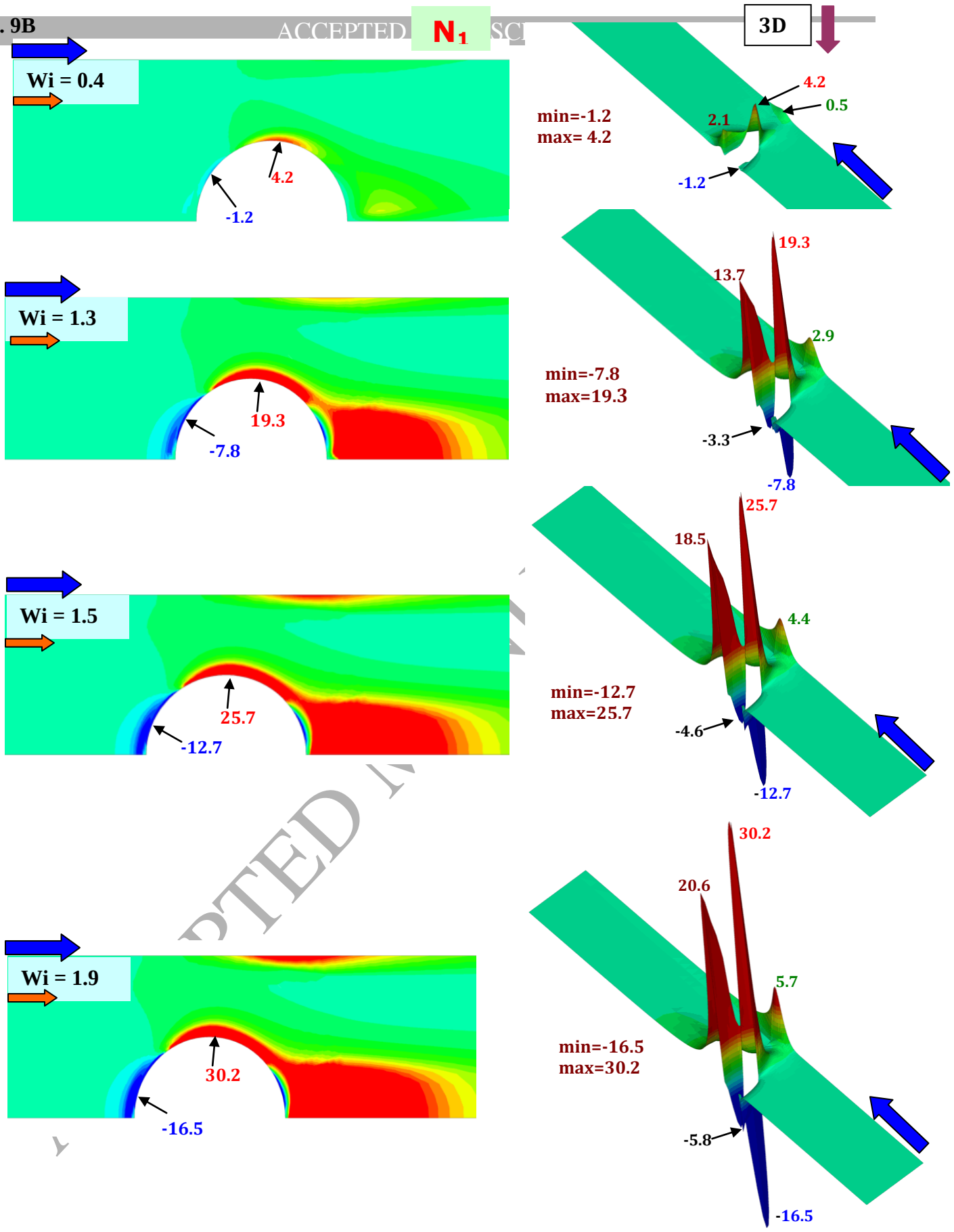
N1
3D
Wi = 0.4
4.2
-1.2
min=-1.2
max= 4.2
4.2
0.5
2.1
-1.2
Wi = 1.3
19.3
-7.8
min=-7.8
max=19.3
19.3
13.7
2.9
-3.3
-7.8
Wi = 1.5
25.7
-12.7
min=-12.7
max=25.7
25.7
18.5
4.4
-4.6
-12.7
Wi = 1.9
30.2
-16.5
min=-16.5
max=30.2
30.2
20.6
5.7
-5.8
-16.5

Fig. 9C

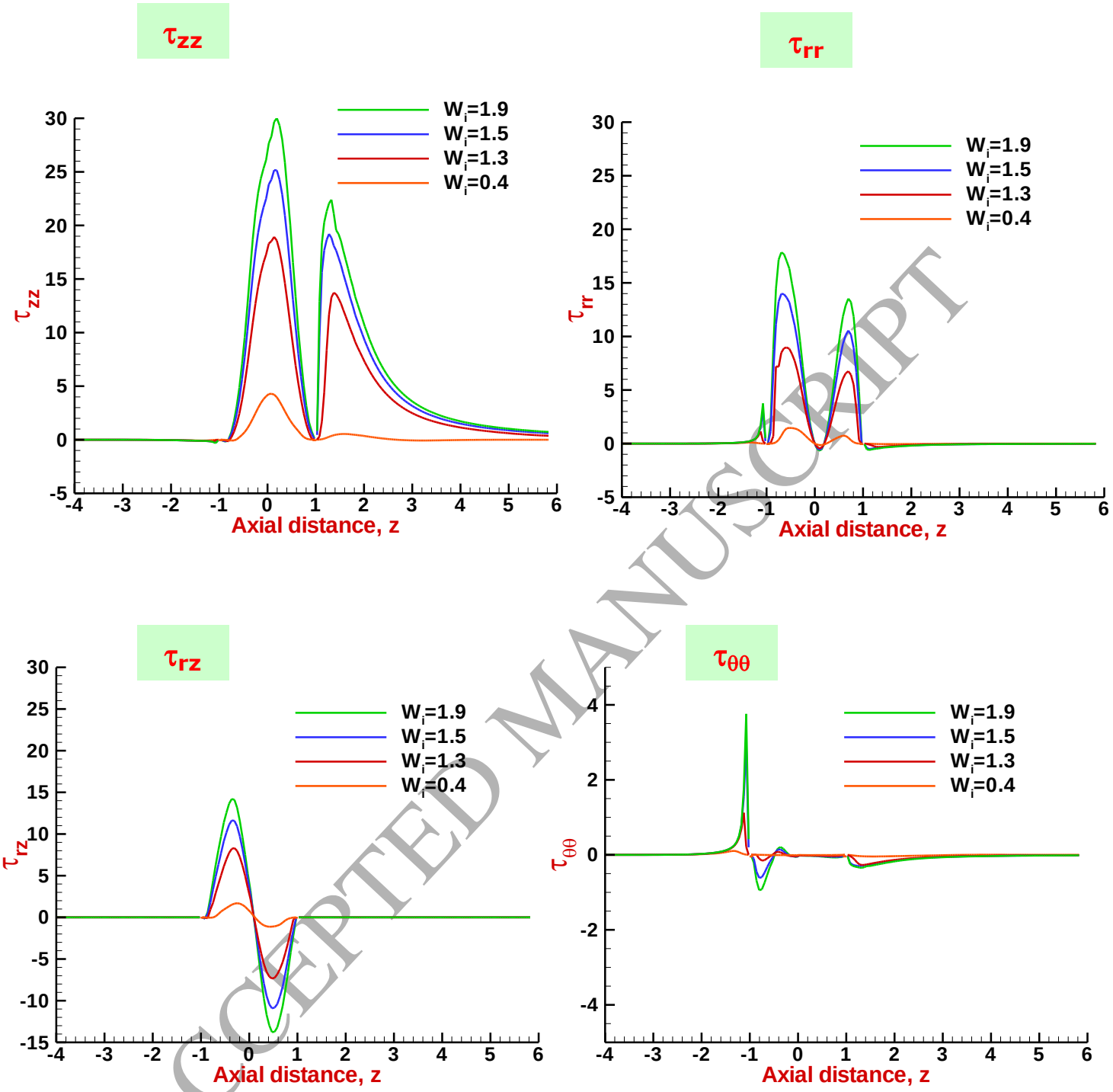

Fig. 9. A) Pressure, B) Normal stress difference (N_1) fields, C) Stress components profiles at centreline and around sphere; various Wi^{Exp}={0.4,1.3,1.5,1.9}, swanINNFM(q) model, L_{FENE} =5, λ_D =0.35, β_{sphere} =0.5

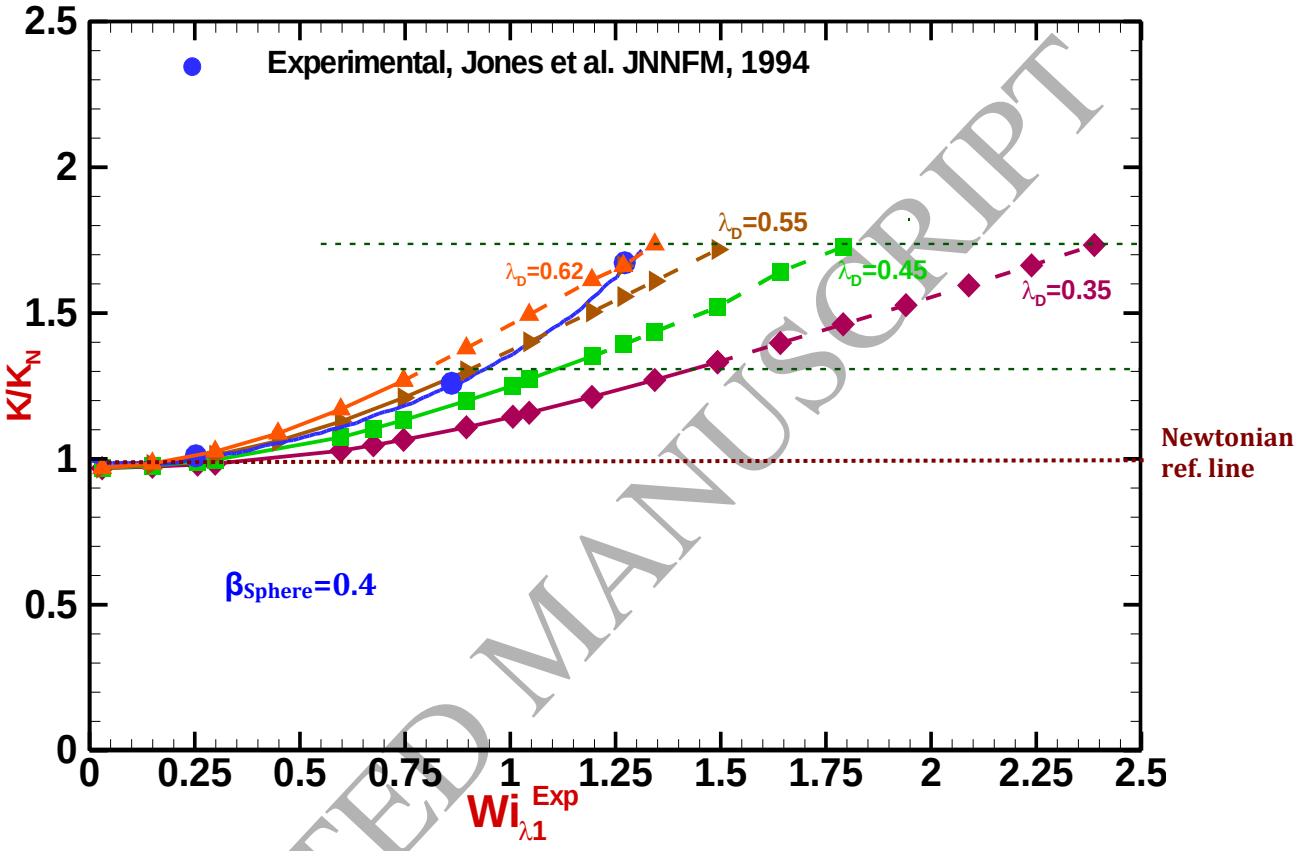

Fig. 10. Normalised *drag coefficient (K/K$_n$)* vs $Wi_{\lambda 1}^{Exp}$, swanINNFM(q) model, L_{FENE} =5, 0.35≤λ_D ≤0.62, β_{sphere} =0.4

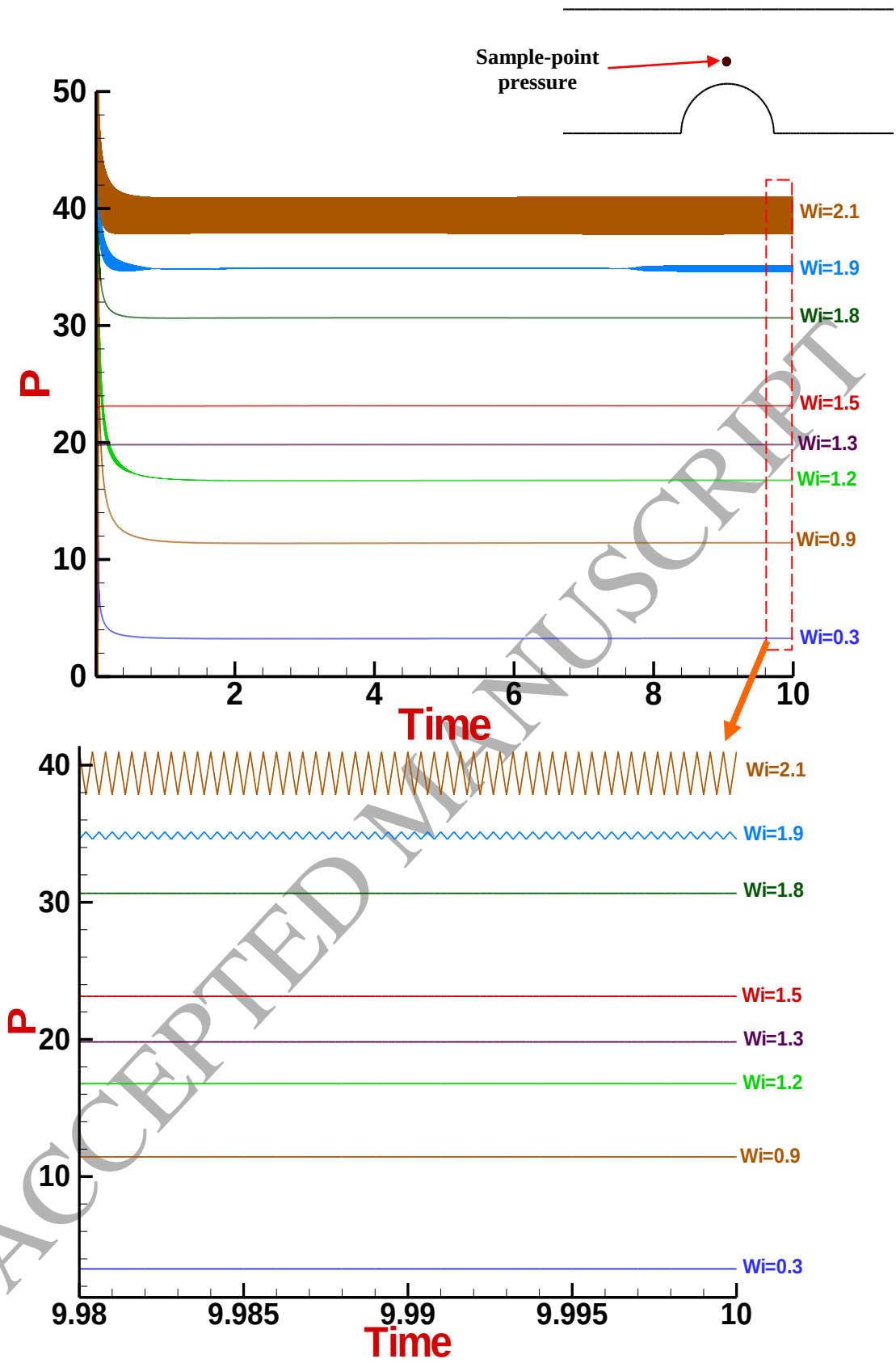

Fig. 11. Sample-point pressure evolution above the sphere (as shown), various Wi^{Exp}, swanINNFM(q), *Q*-increase, λ_D =0.45, β_{sphere} =0.4

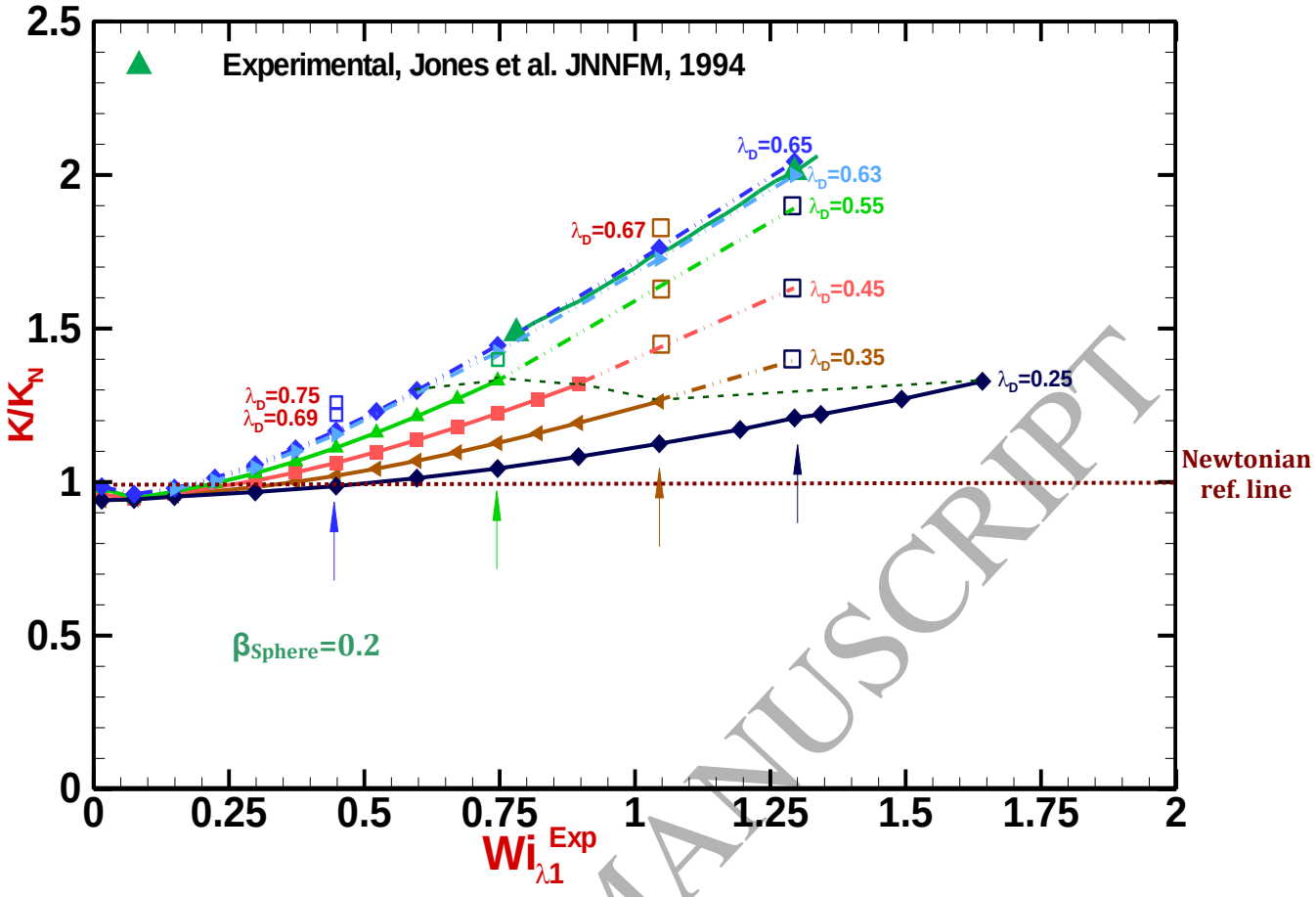

Fig. 12. Normalised *drag coefficient* (K/K_N) vs $Wi_{\lambda_1}^{Exp}$, swanINNFM(q) model, $0.25 \leq \lambda_D \leq 0.75$, $\beta_{sphere}=0.2$

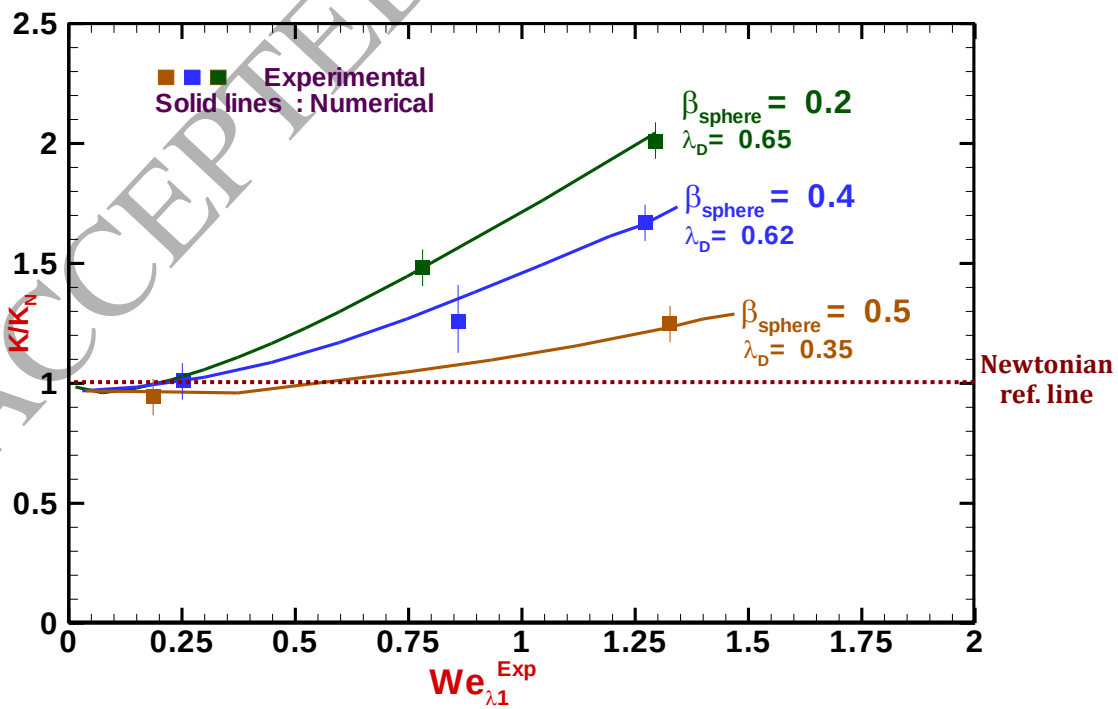

Fig. 13 Drag correction factor (K/K_N), β_{sphere} comparison, experimental data Jones *et al*. (1994) with error bars vs swanINNFM(q) model, $0.35 \leq \lambda_D \leq 0.65$, $\beta_{solvent}=0.9$

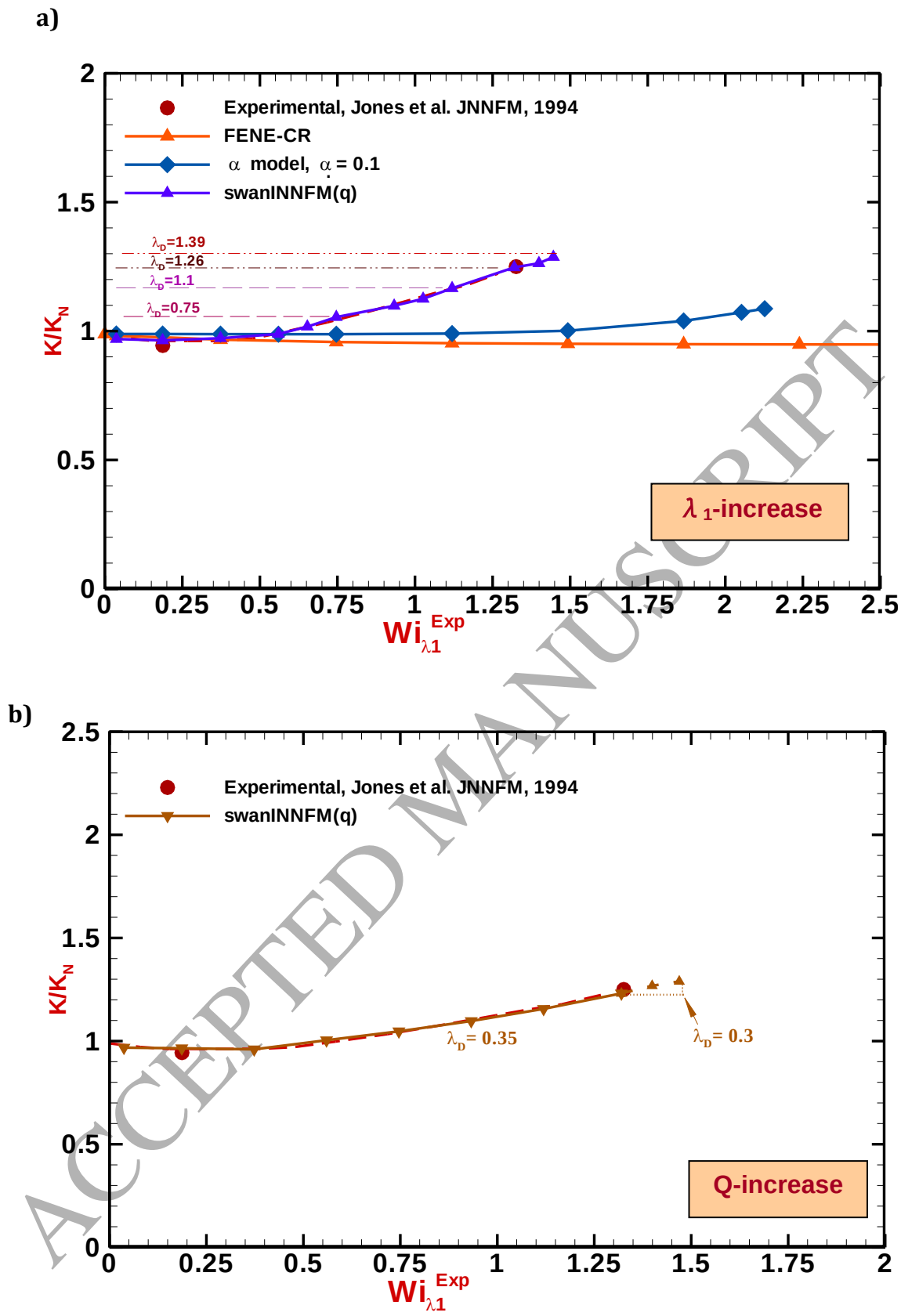

Fig. 14. Normalised *drag coefficient (K/K$_n$)* vs $Wi_{\lambda 1}^{Exp}$, protocol comparison, swanINNFM(q) model, capturing experimental data, a) λ_1-increase, b) *Q*-increase

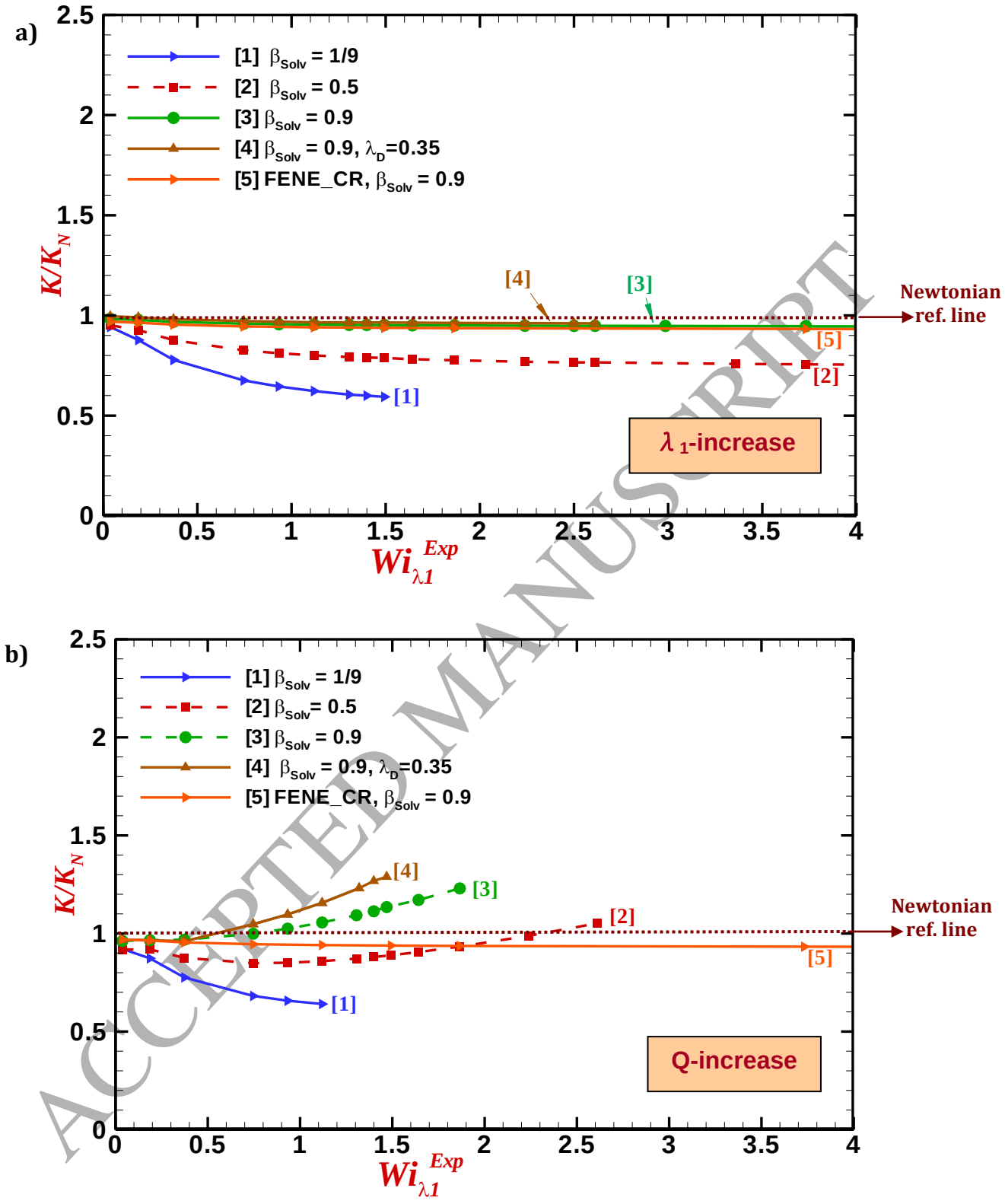

Fig. 15. Normalised *drag coefficient (K/K$_n$)* vs $Wi_{\lambda 1}^{Exp}$, varying solvent-fraction, swanINNFM(q) model, a) λ_1-increase, b) *Q*-increase, λ_D =0.25, $\beta_{solvent}$ =0.9, 0.5, 1/9